Insight into the role of polydopamine nanostructures on nickel foam-based photothermal materials for solar water evaporation

Idris Ibrahim[a], Sayed Mukit Hossain[a], Dong Han Seo[a,b], Andrew McDonagh[c], Tim Foster[d], Ho Kyong Shon[a,e], Leonard Tijing[a,e,*]

[a]Centre for Technology in Water and Wastewater, School of Civil and Environmental Engineering, University of Technology Sydney, PO Box 123, 15 Broadway, Sydney, NSW, 2007, Australia

[b]Energy Materials & Devices, Korea Institute of Energy Technology (KENTECH), Naju, Republic of Korea

[c]School of Mathematical and Physical Sciences, University of Technology Sydney, Ultimo 2007, Australia

[d]Institute for Sustainable Futures, University of Technology Sydney, Ultimo, NSW, Australia

[e]ARC Research Hub for Nutrients in a Circular Economy, University of Technology Sydney, PO Box 123, 15 Broadway, Sydney, NSW, 2007, Australia

[*]Corresponding author: L.D. Tijing; email: leonard.tijing@uts.edu.au

Highlights

- Nano-polydopamine structures on porous nickel foam were prepared via *in situ* synthesis.
- The fabricated solar evaporator improved the photothermal conversion characteristics.
- Good evaporation rate of 1.39 kg m^{-2} h^{-1} and efficiency of 87.6% were obtained.
- The prepared evaporator displayed good reusability and anti-salt properties.

Abstract

This study developed a solar evaporator by uniformly growing polydopamine nanowires (PDA NWs) on porous nickel foam (NF) substrate using a straightforward *in situ* approach. The synthesized material exhibited unique nanostructures, substantial hydrophilicity, and high porosity resulting in excellent light harvesting covering the main solar spectrum. In addition, the utilized polystyrene foam support and cotton cloth resulted in a fast water supply to the evaporator along with heat localization. Good solar water evaporation rate of 1.39 kg m^{-2} h^{-1}, with a photothermal conversion efficiency of 87.6 % was achieved at one sun (1 kW m^{-2}) illumination. The PDA NWs-NF evaporator displayed high-efficiency toward salt ions rejection and met the standard required for potable water. The synthesized material displayed good reusability and stability performance in real seawater and brine (75 g/L NaCl). The self-cleaning properties of the prepared evaporator are driven via chemical advection and diffusion, resulting to fast salt dissolution. Our approach in fabricating cost-effective, scalable and environmentally friendly solar-thermal converter could meet the practical needs for solar-driven seawater desalination especially for remote communities.

Keywords: Polydopamine, Nickel foam, Nanostructures, Solar water evaporation, Seawater desalination

1. Introduction

Around 900 million people living in rural regions with incomes below one dollar per day are unable to obtain freshwater [1]. This leads to hygiene and health impacts, particularly through diarrhoeal diseases [2]. Only about 0.8% of all water sources on the earth's surface are fresh and available as rivers, lakes, and groundwater. Fortunately, seawater is an abundant natural and nearly inexhaustible resource covering three-quarters of the earth's surface [3]. Hence, thermal desalination could be a viable approach to obtain freshwater from seawater. The common technologies used for thermal desalination include multistage flash (MSF) and multi-effect distillation (MED), which are not practical due to costs associated with small-scale applications [4].

The nano-enabled driven-interfacial solar water evaporation has attracted tremendous attention as cost-effective, scalable, and affordable technologies to overcome freshwater scarcity issues [5-7]. This technology is mainly based on photothermal materials (PTMs) to harvest solar energy at the air-water interface and convert it to heat for water evaporation and purification applications [8, 9]. To be an effective solar evaporator, the technology needs to display a high ability for salt rejection even with high saline brine solutions to meet the required standard for potable water [10, 11]. Early studies focused on improving solar absorption, light-to-heat conversion, and water vapor generation, and significant progress has been made in these areas [12]. Recently, research efforts have focused on developing effective solar harvester PTMs with anti-salt properties [13-15]. Salt accumulation on the evaporator surface can block pore channels, causing a substantial reduction of effective surface area for solar absorption. As a consequence, the water evaporation rate reduces significantly [5, 8, 16, 17].

Recently, PTMs with microporous structure and hydrophilic properties have been demonstrated as anti-salt PTMs and excellent solar-thermal conversion materials. A number of substrate materials for PTMs have been studied including porous ionic polymer [18, 19],

biomass structural materials [20, 21] and porous metal foam. Among the reported materials, NF has been well reported as an excellent substrate to grow versatile nano or microstructured materials [22]. It possesses a 3D porous structure with an open network and substantial surface functionality for growing different nano/microstructures materials [23]. These unique features make it highly desirable for an anti-salt and reusable solar evaporator system. To date, various NF based materials have been reported including $CoWO_4$-x@NF [24], nickel sulfide@NF [25], graphene foam [26], graphene/MoO_3-x@NF [27], and Fe_2O_3/CNT@NF [28]. Other studies have shown that bio-inspired polydopamine (PDA) is an effective PTM with owing to its advantages of simple synthesis methodology via *in situ* self-polymerization processes and a functionality to grow on various substrates [29-31]. PDA exhibited a broad spectrum of light absorption due to the adequate conjugated structures given by indole-5,6 quinone. Furthermore, the chemical bonds between the 5,6-dihydroxyindole and indole-5,6 quinone units are considered to operate as electron donor and acceptor pairs, influencing the energy bandgap and light absorption properties [31-33].

Hence, in this work, we report a series of PDA nanostructures on porous nickel using a simple *in situ* synthesis method. The resultant materials exhibit excellent solar light absorption and efficient water transmission. A simple solar evaporator was fabricated, which contains cotton cloth as a 2D water transport channel to ensure a continuous water supply and cover on PS foam to act as a thermal insulator. The prepared evaporator displayed effective solar light absorption and solar-thermal conversion, with the continuous water pumping to PDA nanowires (NWs)-NF, resulting in an evaporation rate of 1.39 kg m^{-2} h^{-1} and an efficiency of 87.6 %, under 1 sun intensity. The applications of the solar evaporator in solar seawater desalination were demonstrated with high salt rejection to obtain potable water which meets the World Health Organization (WHO) standard. Furthermore, the PDA NWs-NF displayed good reusability with stable performances for 3 days under real seawater and high brine salinity (75g/L NaCl). Finally, self-cleaning properties were proved in this study. This work

demonstrated a novel, low-cost, highly stable, anti-salt solar evaporator system with a potential application for seawater desalination.

2. Experimental procedures

2.1 Materials

Nickel foam (Purity: 99.99%) was bought from MTI Corporation-USA. Dopamine hydrochloride (Purity: ≥ 99.0%) and Tris(hydroxymethyl)aminomethane (Tris-base) (Purity: ≥ 99.8%) were purchased from Sigma-Aldrich.

2.2 Synthesis of PDA nanostructures on nickel foam

In this study, PDA nanostructures were synthesized using a modified method from [30] to produce new and unique structural morphology. A piece of NF (size: 5 cm x 5 cm) was washed with distilled water, ethanol and immersed in 1 M HCl for 1 h to remove the oxide layer. The treated foam was then immersed in a solution (Tris-buffer pH 8.5) containing dopamine (2 mg/mL), and the total amount of solution was 200 mL. The Tris-buffer was prepared by dissolving 121.15 g/mol of Tris(hydroxymethyl)aminomethane in 1L of water, and the pH was adjusted to 8.5 by adding concentrated HCl. The solution was stirred for 2 and 6 h at ambient temperature. The as-prepared PDA nanostructures on NF were rinsed with distilled water and kept for further use. **Fig. 1** illustrates the process of the formation of grown PDA nanoparticles (NPs) within 2 hours reaction time. While the PDA nanowires (NWs) formed on NF surfaces after stirring for 6 hours.

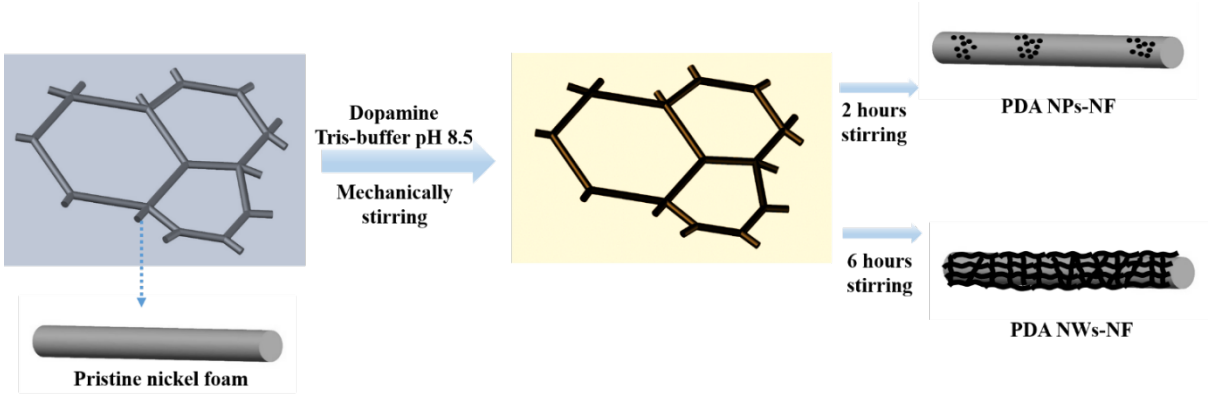

Fig. 1 Schematic of the fabrication process of PDA nanoparticles and PDA nanowires (NWs) on NF.

2.3 Characterization

The surface morphology of polydopamine nanostructures on the NF surface was investigated using a scanning electron microscopy (SEM, Zeiss Supra 55-VP) at an accelerated voltage of 5 kV. The energy dispersive spectroscopy (EDS) and elemental mapping were measured using SEM (Zeiss EVO SEM) at 15 kV. The surface wettability of the samples was investigated by Theta Lite 100 (Attension) using a sessile drop method. The light absorption characteristics of the pristine NF and prepared materials were measured using a spectrophotometer equipped with an integrating sphere (950 PerkinElmer Lambda) at wavelength range (300-2500 nm; Ultraviolet-Visible-Near-Infrared regions). The positively charged ions (K^+, Na^+, Mg^{2+}, and Ca^{2+}) concentrations of the condensate water were measured using an inductively coupled plasma mass spectrometer (Agilent 7900 ICP-MS). A Thermal Advantage SDT-Q600 thermal analyzer was used to obtain TG curve using alumina crucibles. Experiments were conducted using a flow of nitrogen gas (150 ml min^{-1}) and a heating rate of 10 °C min^{-1} over a temperature range of 25-500 °C.

2.4 Solar water evaporation experiments

Solar water evaporation tests were conducted at ambient temperature (24 °C, humidity 60%) under solar irradiation of 1 sun using a solar simulator (Beijing Perfect Light) equipped with a filter (AM 1.5).Solar evaporator composed of PDA nanostructure/NF was cut into a circular shape (Diameter ~ 3.4 cm) and was placed at the top of the cotton cloth (2D water channel) wrapped polystyrene foam (thermal insulator) in a beaker filled with 35 mL of deionised water (DIW). Photo-image of the solar evaporator device is given in **Fig. 2 a, b and Fig. S1.** Upon sunlight irradiation on the solar evaporator, the weight change was measured using an electronic balance (Ohaus-IC-PX84/E) at an interval of 4 min and the total time of each test is 1 h. The temperature and thermal distribution on the solar evaporator and the water was visualized and measured using an infrared camera (FLIR E6).

(a)

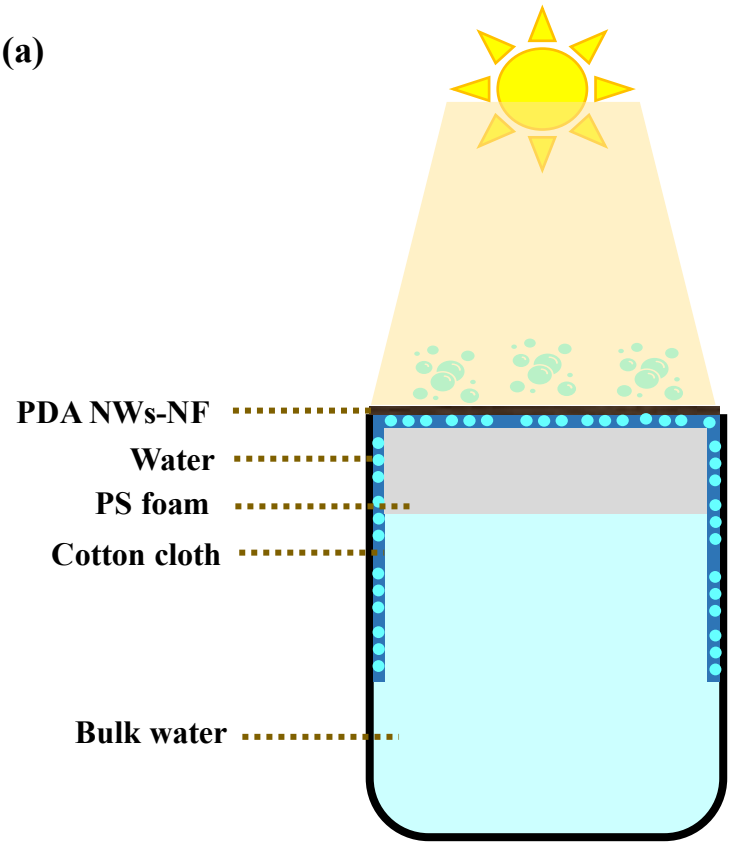

(b)

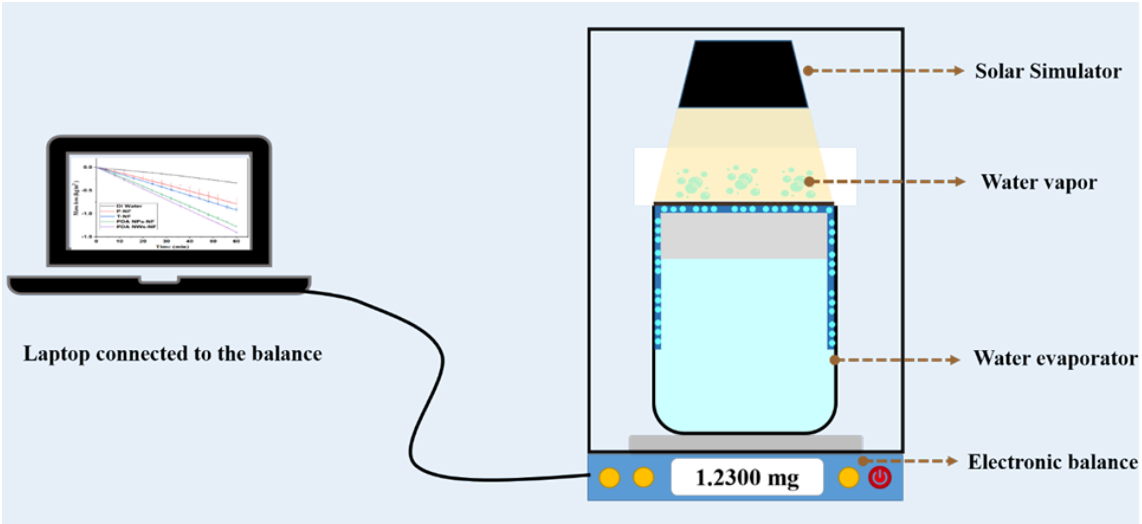

Fig. 2 Schematic illustration of the **(a)** designed solar evaporator system, and **(b)** solar water evaporation set-up.

2.5 Solar desalination test

The solar desalination performance was evaluated using seawater collected from Rose Bay Beach, Sydney, and similar protocols for SWE were followed. The seawater was filtered using a coarse filter, followed by a 5-micron bag filter, then treated with UV light before use. River water collected from Brago River (Wollongong, Australia) was also used as source water. During solar desalination tests, the evaporated water was collected and analyzed using ICP-MS to measure the ions of the feedwater and the purified water. Furthermore, the cycling stability tests were carried out for 3 days and 5 cycles per day using seawater and simulated high brine solution of NaCl (at 75 g/L). Details on salt crystallization were performed using SEM and EDS analysis.

3. Results and discussions

3.1 Characterizations

Fig. 1 illustrates the process of the formation of the grown PDA nanoparticles (NPs) and PDA nanowires (NWs) on NF surfaces. Before the growing of PDA nanostructure on NF, the NF

surface underwent a surface treatment to remove the oxide layer. Then, PDA was grown directly on the treated NF surface using a straightforward process that takes place through the oxidation of dopamine using a Michael addition reaction (**Fig. S2**) [30]. During the reaction process, the color of the solution changed from light brown to dark brown which confirmed the oxidative polymerization of the DA to PDA [30] corresponding to an increase in amount and thickness of PDA on the NF [34]. The photographic images of the pristine NF, treated NF, and coated NF with PDA are given in **Fig. S3.**

Fig. 3 shows the SEM and EDS results of the treated NF absorbers (see **Fig. S4** for the SEM images of pristine NF). After 2 h reaction, the SEM results confirmed the formation of PDA aggregated nanoparticles (NPs) with an average size of about 50 nm **(Fig. 3 (a-c))**. After extending the reaction time to 6 h, the NPs on the surface self-assembled into NWs with hierarchical structures which were uniformly distributed on the surface of NF, as shown in **Fig. 3 (d-f)**. The formation of the NWs can be explained by the π- π stacking interactions promoted by sufficient conjugated structures of PDA NPs to assemble PDA NWs on the NF surface. The EDS analysis revealed the existence of the PDA elements (Ni, C, N, and O) on NF (Ni). Furthermore, the elemental percentages in PDA NWs-NF were higher than PDA NPs-NF (**Fig. S5 and S6**). The elemental mapping confirms the homogeneous distribution of C, N, and O, which was more abundant on Ni foam, while C, N, and O within PDA NPs are less and inhomogeneously distributed. Thermogravimetric analysis (TGA) of PDA grown on NF substrate was performed from ambient temperature to 800 °C. As shown in **Fig. S7**, the thermal loss curve displays multiple mass losses. Between 25 °C to 100 °C, the mass loss event is attributed to the removal of moisture on the surface. The curve for pristine NF was stable until 500 °C, and then it started rising owing to the conversion of pristine nickel to nickel oxide. Meanwhile, the coated NF with PDA showed a mass loss of ~ 3.08% and ~ 1.6% at 490 °C for

PDA NWs-NF and PDA NPs-NF, respectively. The higher percentage of decrease of PDA NWs is due to the higher concentration of PDA on the NF surface.

.

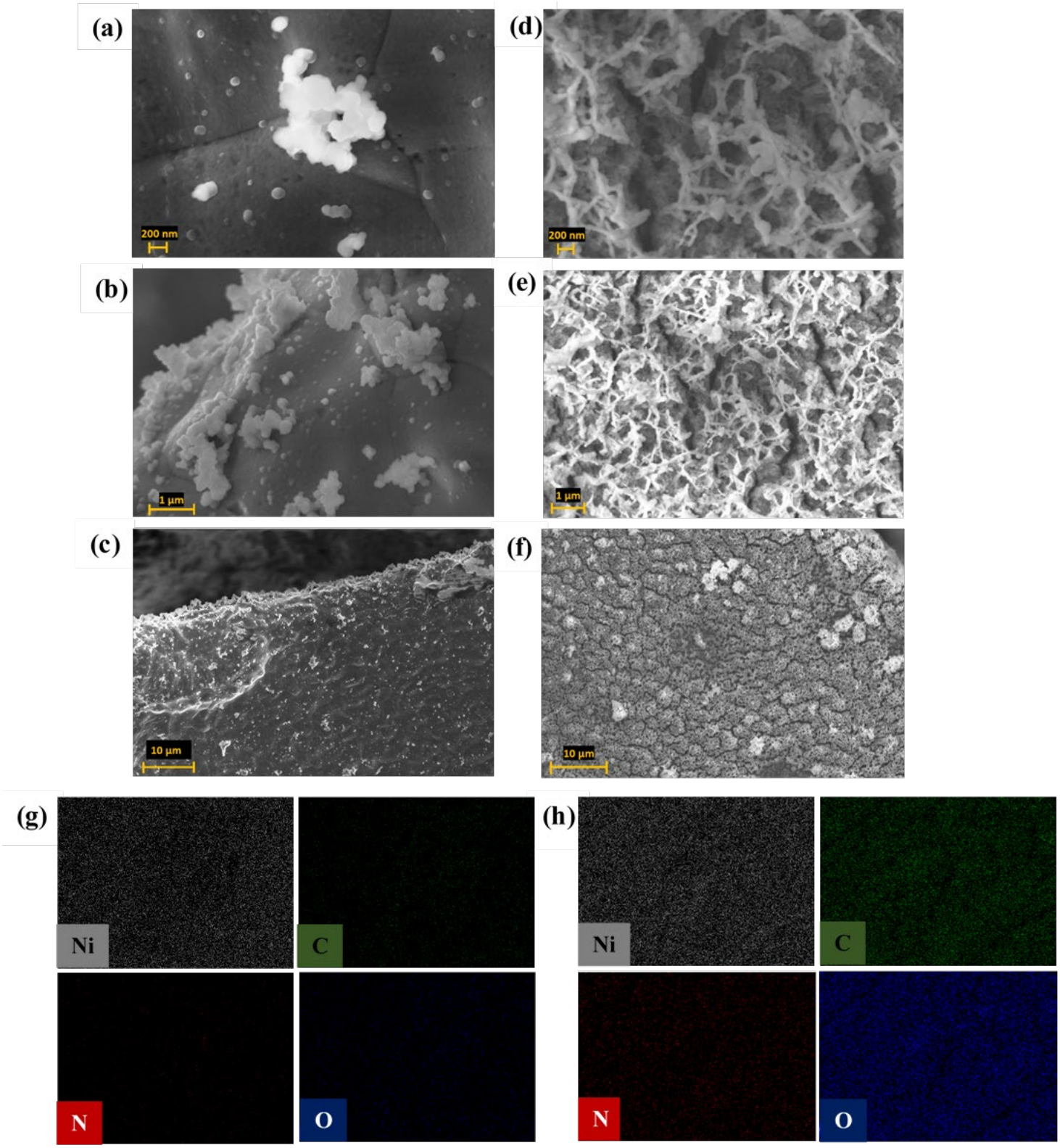

Fig. 3 SEM images of (a-c) PDA NPs-NF. (d-f) PDA NWs-NF. (g) Elemental mapping of PDA NPs-NF. (h) Elemental mapping of PDA NWs-NF.

3.2 Surface wettability and water transport

Surface wettability is an important criterion to ensure fast and effective water penetration and transportation within the structures of PTMs during the water evaporation test. A water contact angle of 131° was obtained for the pristine NF (**Fig. 4 (a)**). Upon surface treatment, the wettability was enhanced, and the water contact angle reduced to 113° **(Fig. 4 (b))**. The reduction in contact angle is attributed to the removal of the oxide layer from the NF surface. After the PDA coating process, the wettability changes from hydrophobic to superhydrophilic. Therefore, water penetrates and spreads rapidly within the surface within 1.38 s for PDA NPs-NF and 0.40 s for PDA NWs-NF **(Fig. 4 (c-d))**. This ultrafast water spreading is due to the hydrophilic hydroxyl-containing functional groups in PDA [35]. The water transport for PDA NWs-NF was faster than PDA NPs-NF due to the thicker PDA on the NF surface.

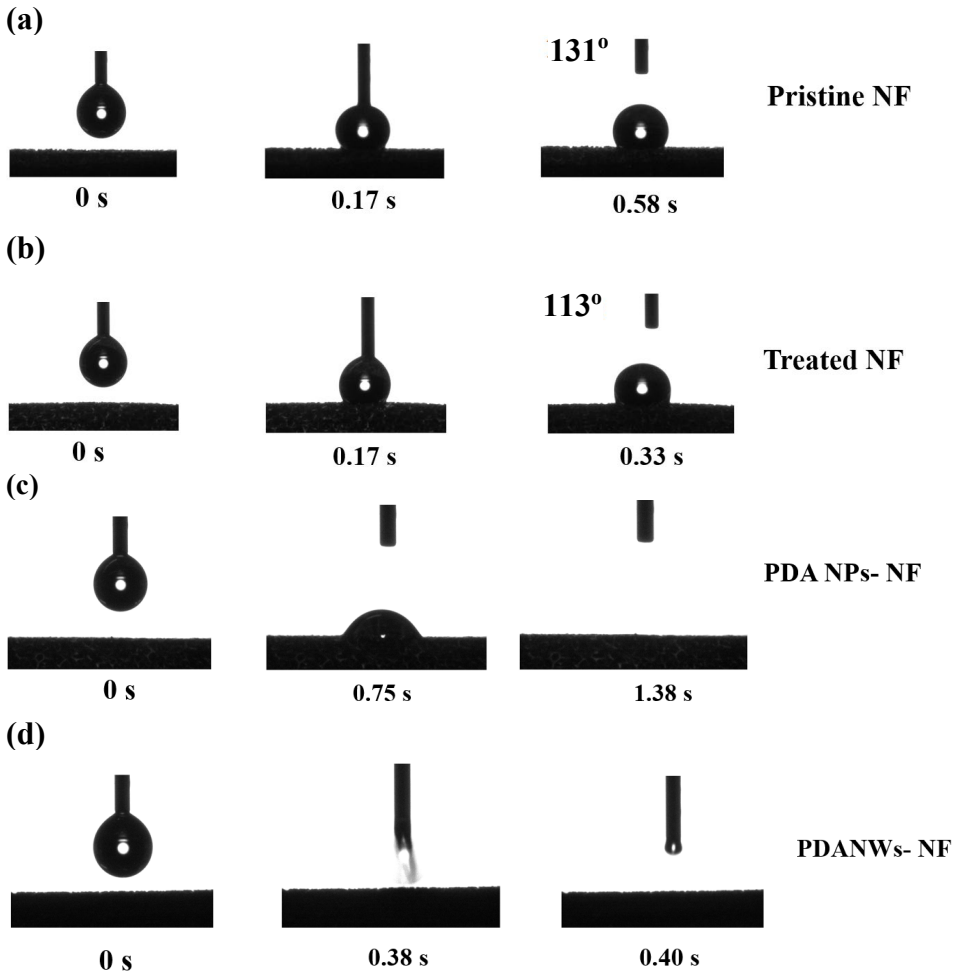

Fig. 4 Contact angle measurement of; (a) P-NF, (b) T-NF, (c) PDA NPs-NF, and (d) PDA NWs -NF.

3.3 Light absorption properties

The ability of the PTMs to absorb solar light is essential for a highly efficient solar evaporator system [36]. We examined the light absorption in the dried state (**Fig. 5 (a)**) and wet state (**Fig. 5 (b)**) over a wavelength range covering the bulk of the solar spectrum (300-2500 nm), (UV; 300-600 nm, Vis; 600-750 nm, NIR; 750-2500 nm). The optical absorption results clearly display the capability of NF and PDA coated NF to efficiently absorb the sunlight across the solar spectrum which is an important criterion for efficient solar-thermal conversion in solar water evaporation [36]. The superior light absorption is attributed to the high porosity and 3D interconnected structures of the foam yielding high light absorption through multiple internal scattering and trapping results in less reflections and transmittance [14, 37]. The pristine NF displays light absorption of ~68-73% in the UV region, ~56-73% in the visible light region, and ~38-56% in the NIR region. In contrast, the treated NF shows better absorption capability (~73-77 %) at UV, (~ 66-73%) at Vis, (41-66%) at NIR. The results for the pristine NF are consistent with previous investigations [14, 38, 39]. The reflections and transmittance results are shown in **Fig. S8**. The light absorption was increased after coating NF with PDA NPs reaching ~ 85%, 76-85%, 52-76% at UV, Vis, and NIR regions, respectively. The improved in the absorption capability is attributed to the strong π-π interactions on PDA compounds [40]. The light absorptions can be further extended by increasing the thickness of PDA by forming hierarchical NWs on NF surface to finally reach (~90%) at UV, (~90-88%) at Vis, (59-88%) at NIR. The formed porous hierarchical structures can help enhance light harvesting through multiple scattering [25]. Furthermore, light absorption was investigated at the wet state to validate the influence of the absorbed water on the light capturing ability, as the evaporation will take place under water [36]. Interestingly, the light absorption is further boosted at the wet

state, mainly in the NIR regions, which could be attributed to the porous hydrophilic structures' capability to allow more water within the pores. Water replacing the air within the pores is well-known to further extend the light absorption capability in the NIR regions [41]. To validate this, the untreated NF (hydrophobic) displayed lower light absorption compared to the treated NF. These trends in the optical performance are similar to our previous report [42] and other reported work [43-45]. The results demonstrate that the superhydrophilicity and high porosity structures are important factors for enhancing the light absorption characteristics, which is beneficial for solar-thermal conversion. A schematic illustration of the mechanism of absorption of our designed solar evaporator is provided in **Fig. 5 (c)**.

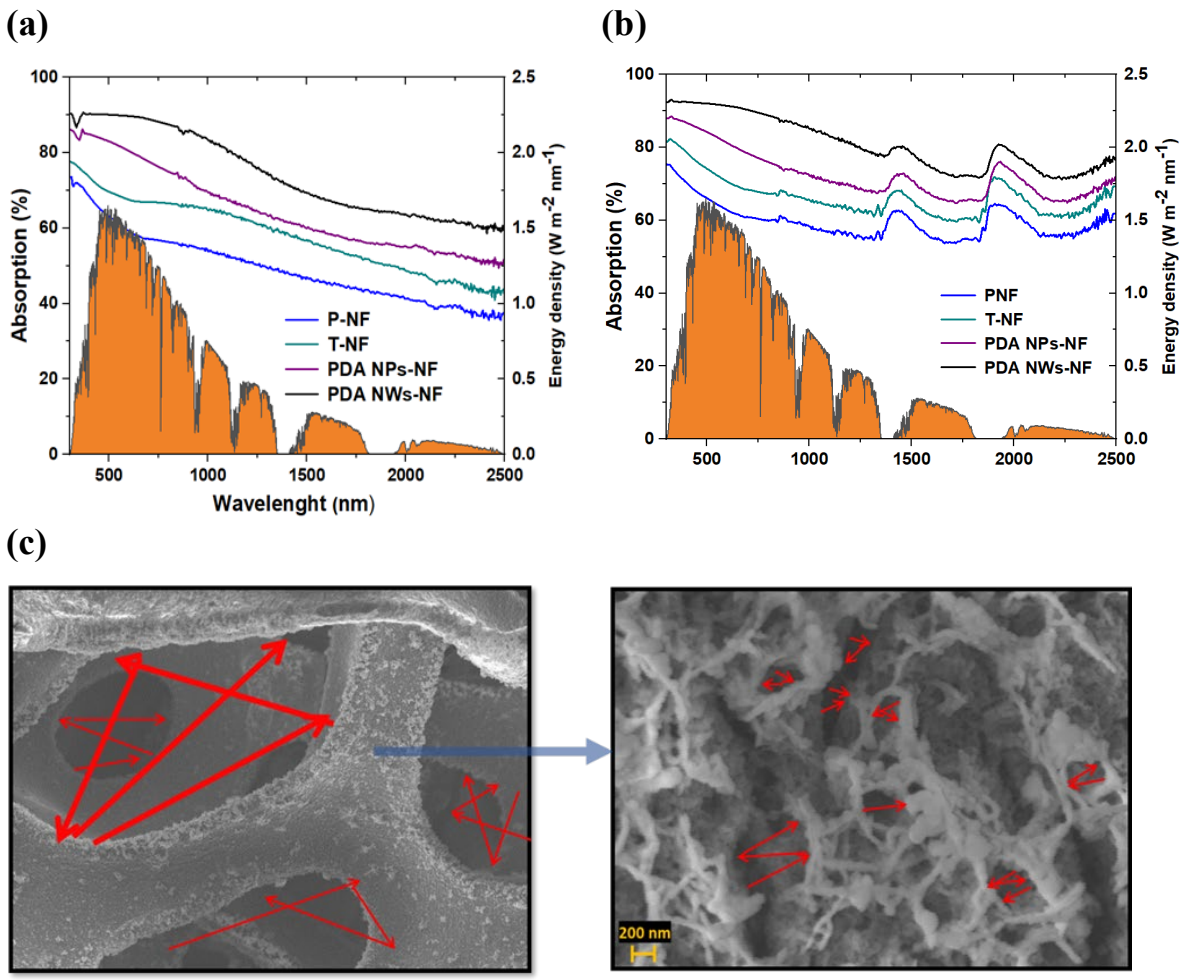

Fig. 5 Light absorption and heat conversion characteristics of NF substrates and after coating with PDA nanostructure for the dry state (a) and wet state (b) at the UV–vis–NIR spectra and

solar energy density spectrum (orange). (c) The light reflection pathway between the pores of nickel foam (left image) and nanowires on NF (right image).

3.3 Solar photothermal conversion

A solar evaporator was constructed that was composed of a solar absorber (P-NF, T-NF, PDA NPs-NF, and PDA NWs-NF) on top of a thermal insulator PS foam wrapped with cotton cloth as 2D water transport (see **Fig. S1)**. The cotton cloth allowed fast water transport from the bulk water to the evaporator surface. Hydrophobic PS foam acts as a supporter and thermal insulator. The designed device allowed fast water transport and water vapor escape, while the heat is localized at the air/water interface resulting in efficient energy utilization and improved water evaporation performance.

An IR camera was used to investigate the solar-to-thermal conversion of the PTM and thermal insulation capability of the designed evaporator. Thermal images of the top surface were collected until it reached an equilibrium temperature within 900 s. The resultant PDA NWs-NF was compared to the PDA NPs-NF, T-NF, P-NF, and DIW. **Fig. 6 (a) and (b)** show that the surface temperature of all samples rapidly increased within 4 min, then steadily stabilized after 10 min of solar illumination. In the case of the baseline DIW based evaporator, the surface temperature increased gradually from 23 to 25.7 °C within 15 min. In contrast, the surface temperature of our evaporators attained a temperature above 32 °C, which is sufficient to generate water vapor. This can be explained by the 3D interconnected porous structure of the NF, which potentially results to localizing the heat in the evaporation area [14]. This also will

In brief, the surface temperature for P-NF and T-NF rose from 21.8 °C and 19.1 °C to 27.6 °C and 32.3 °C, respectively within 3 min, and goes up to 32.5 °C to 35.7 °C after 15 min. However, the coated NF with PDA display high solar-thermal conversion, and for the PDA NPs-NF and PDA NWs-NF, temperatures rise rapidly from 18.8 °C and 19.6 °C to 31.9 °C and

295 34.2 °C within 3 min. and continued to increase to 36.1 °C and 39.5 °C within 15 min. The
296 rapid photothermal response of PDA NWs-NF is 3.4 °C higher than PDA NPs-NF owing to
297 the hierarchical nanowires structures resulting in more heat-trapping on the surface. This fast
298 photothermal response is beneficial for reducing time for warming up the evaporator surface
299 for vapor generation [46]. In contrast, the side-view of the PDA NWs-NF evaporator shows
300 the interfacial heat localization at the top region and low surface temperature of the bulk water
301 (**Fig. S9**), which indicates good thermal insulation properties from PS foam resulting in
302 localized heat at the top surface on the nanostructure PDA-NF surface [42]. Consequently,
303 excellent solar-thermal conversion in a high-performance solar water evaporation system was
304 achieved.

(a)

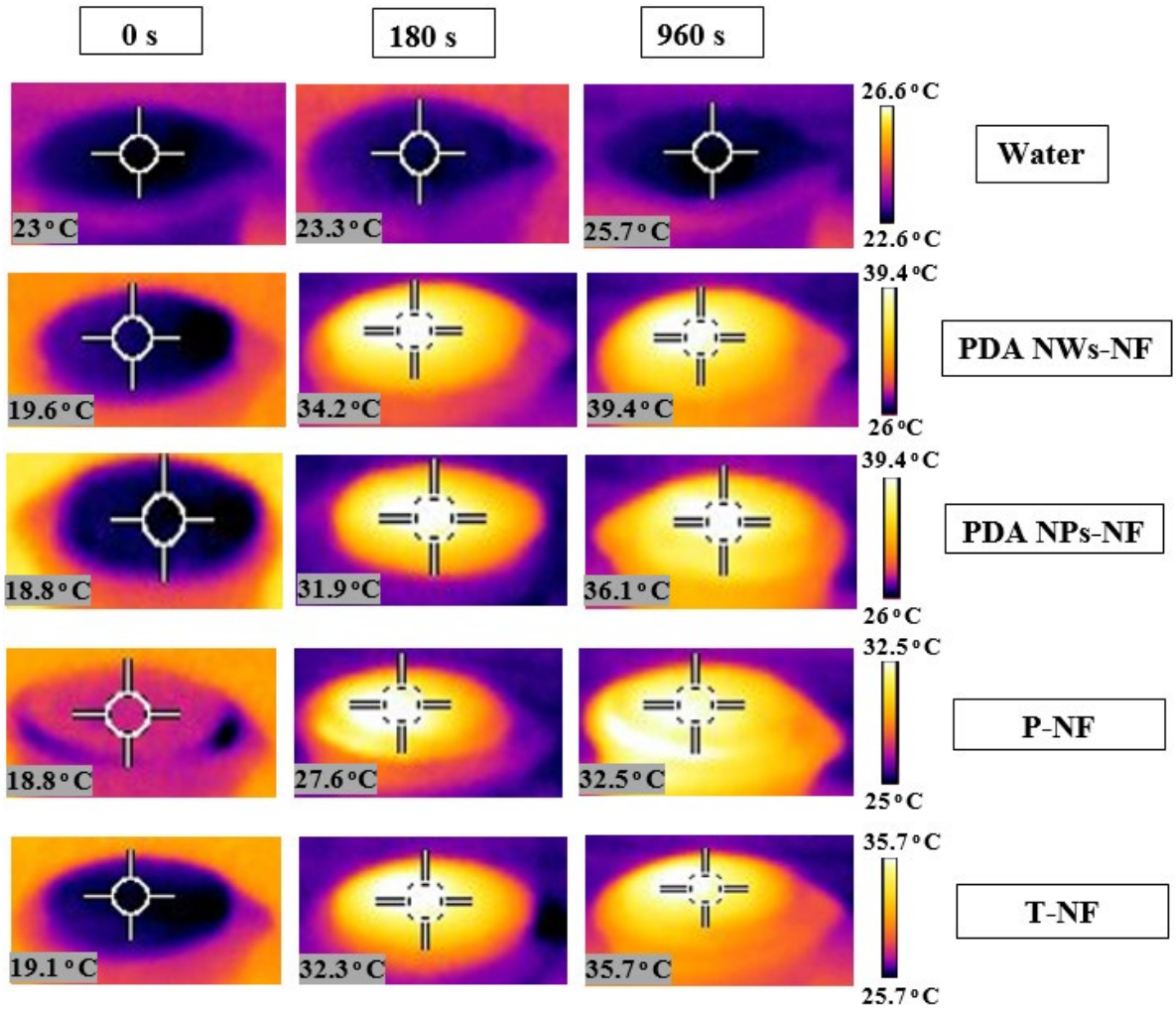
0 s
180 s
960 s
23 °C
23.3 °C
25.7 °C
26.6 °C
22.6 °C
Water
19.6 °C
34.2 °C
39.4 °C
39.4 °C
26 °C
PDA NWs-NF
18.8 °C
31.9 °C
36.1 °C
39.4 °C
26 °C
PDA NPs-NF
18.8 °C
27.6 °C
32.5 °C
32.5 °C
25 °C
P-NF
19.1 °C
32.3 °C
35.7 °C
35.7 °C
25.7 °C
T-NF

(b)

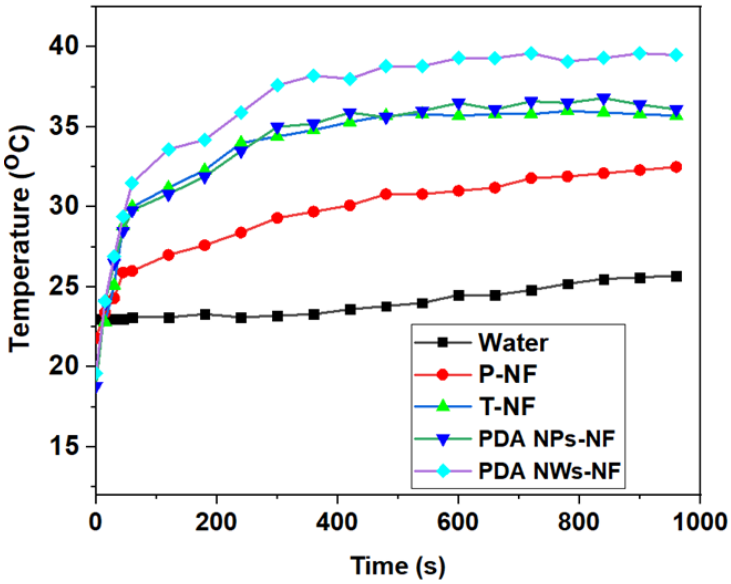
Temperature (°C)
Time (s)
40
35
30
25
20
15
0
200
400
600
800
1000
Water
P-NF
T-NF
PDA NPs-NF
PDA NWs-NF

305

Fig. 6 Light absorption and heat conversion characteristics of NF substrates and after coating with PDA nanostructure. (a) IR images revealed the effectiveness of PDA nanostructure based solar evaporator in localizing heat at the air-water interface. (b) Temperature profile of heat conversion with respect to time.

3.4 Water evaporation performance

Water evaporation performance was evaluated under one sun intensity and the mass change was recorded at 4 min intervals with a duration of 1 h for each test. The evaporation rate was calculated from the slope of the curve. The evaporation rate at the dark condition was subtracted before calculating the efficiency**.** The solar heat-to-vapor efficiency (η) is calculated using the equation below [37, 47]:

$$\eta = \frac{\Delta \mathrm{m} * He}{I * T} \qquad [1]$$

where Δm ($m_i - m_o$) m_i is the water mass change (kg/m^2) under solar light, and m_o is the water mass change (kg/m^2) at dark (without sunlight), I is the solar power energy density (kW m^{-2}), T is the irradiation period (3600 seconds), while, He is the total vaporization enthalpy of the water-steam phase change (kJ·kg^{-1}).

Fig. 7 (a-d) show the mass loss, water evaporation rate, and calculated efficiency data results. The data show that the DIW based evaporator has a low evaporation rate of 0.33 kg m^{-2} h^{-1}, corresponding to an efficiency of 14.4%. Our interfacial solar evaporator-based P-NF and T-NF displayed water evaporation rates of 0.79 kg m^{-2} h^{-1} and 0.92 kg m^{-2} h^{-1}, with efficiencies of 43.5% and 52.9%, respectively. The higher evaporation rate of T-NF is attributed to the enhanced surface wettability that enabled fast water transportation during evaporation. The trends seen here also reflect those of the optical data. After coating NF with PDA NPs, the water evaporation rate was further enhanced to achieve evaporation of 1.27 kg m^{-2} h^{-1} and an efficiency of 75.9%. PDA NWs-NF showed an evaporation rate of 1.39 kg m^{-2} h^{-1}, and an

efficiency of 83.3%, about 4.2 times higher than DIW. The increase in water evaporation rate of PDA NWs-NF could be attributed to the following four features:

a) The superhydrophilicity of the PDA acted as water transporter and solar-thermal converter.

b) The larger quantity of PDA NWs-NF resulted in high capability of solar-thermal conversion and faster water supply compared to the lower PDA content in PDA NPs on NF.

c) The 3D microstructures of the NF resulted in more water penetration within the pores, as a result, more water surface was available.

d) The presence of PS foam and cotton cloth leaded to excellent heat localization at the air/water interface and caused adequate water supply.

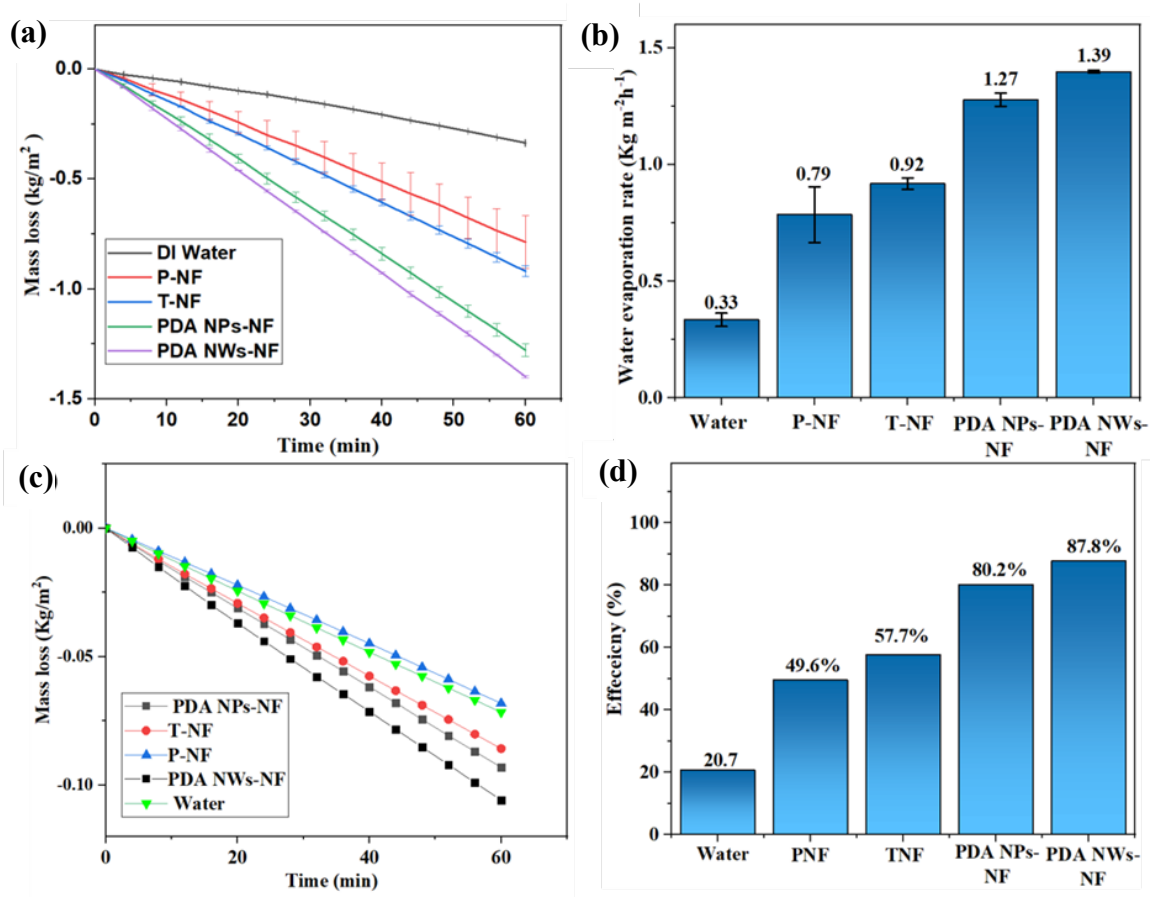

Fig. 7 (a) Weight change with respect to time (min) under 1 sun intensity (1 kW m^{-2}). (b) Water evaporation rate under 1 sun intensity (1 kW m^{-2}) (kg m^{-2} h^{-1}). (c) Water evaporation rate under dark conditions. (d) Water evaporation efficiency (%).

3.5 solar desalination performances

Solar desalination performance was assessed using natural seawater. For water condensation and collection performance, a purpose-built device was used (**Fig. S10).** The principle work of the device is through the sunlight which passing through the beaker which covered our prepared solar evaporator. After the sunlight irradiation the water started to evaporate and condensate on the covered beaker. Then, the compensated water will be collected and quantified. The salt ion rejections of the primary salt ions (Na^+, Mg^{2+}, Ca^{2+}, and K^+) were quantified before and after the desalination test using an ICP-MS instrument. The salt ions were significantly reduced to below 2 mg/L for seawater and river water (**Fig. 8 (a, b**)). The obtained results were far below the standard WHO and the US Environmental Protection Agency (EPA) levels for drinking water. Hence, our PDA NWs-NF based evaporator displays excellent capability in salt ion rejection to produce drinking-quality water.

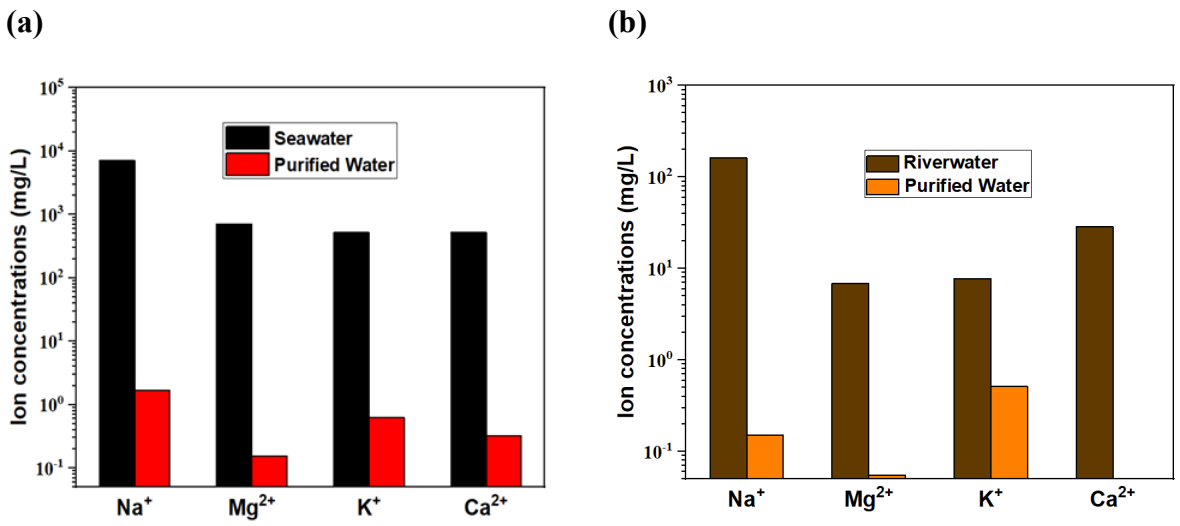

Fig. 8 ICP-MS analysis of the primary salt ion concentrations (Na^+, Mg^{2+}, Ca^{2+} and K^+) before and after solar desalination using PDA NWs-NF based evaporator; **(a)** Seawater. **(b)** River water.

361 The long-term stability and reusability of PTMs is considered vital for practical applications in
362 solar-driven seawater desalination [5, 8]. Salt crystallization on the solar evaporation surface
363 lowers solar-thermal conversion efficiency of PTMs, hence lowering evaporation rates and
364 hindering practical application [12]. In this study, durability and stability tests were conducted
365 using two types of salted water including real seawater and high salinity brine (75 g/L NaCl).
366 Surface morphology and elemental composition of PDA NWs-NF based evaporator were
367 further investigated after 3 days using SEM and EDS analysis. The durability and stability test
368 were investigated under one sun intensity. Tests were carried out for 3 days, with 5 cycles per
369 day (1 h/cycle); after each day, the evaporator was left overnight under dark conditions. The
370 calculated water evaporation results displayed a rate of 1.38 kg m^{-2} h^{-1} and 1.32 kg m^{-2} h^{-1}, for
371 seawater and high brine solution (75 g/L NaCl), respectively, which are closer to 1.39 kg m^{-2}
372 h^{-1} of DIW.
373 The durability test using seawater revealed a stable performance during day 1 and 2, with very
374 slight increase on the third day (**Fig. 9 (a)**). Moreover, after the third day, SEM analysis
375 revealed some salts crystalized and accumulated between PDA NWs on the NF surface, which
376 was confirmed by EDS to be Na, Cl. Mg, Ca, Cl, and S, O, which correspond to the formation
377 of NaCl, $MgSO_4$, $MgCl_2$, $CaCl_2$, and Na_2SO_4 on the surface **Fig. S11 (a-c)**. Then, salt formed
378 on PDA NWs-NF was cleaned by soaking in DIW for a period of 9 h at ambient temperature.
379 As seen by SEM analysis, the salts were removed and the PDA NWs remained intact on the
380 NF surface **Fig. S12 (a-b)**. Furthermore, the EDS analysis confirmed negligible sodium and
381 chloride content, revealing the high removal efficiency of salt crystals from PDA NWs-NF
382 surface **(Fig. S12 (c))**. In contrast, the high salinity solution (75 g/L NaCl) displayed different
383 trends; the evaporation was stable for day one and then started slightly to decrease on day 2
384 and then day 3 to reach an evaporation rate of 1.31 kg m^{-2} h^{-1} (**Fig. 9 (b)**). The SEM images
385 further confirmed the presence of NaCl on the PDA NWs-NF. The SEM images revealed some

parts contained the PDA NWs on the NF surface, while some large NaCl crystals were observed on the surface (**Fig. S13 (a-d)**). Salt was removed from the PDA NWs-NF surface by soaking it in DIW for 9 h at ambient temperature. Notably, it can be seen from the SEM images that no salt on the PDA NWs-NF surface and the PDA NWs remain almost confined on the NF surface **Fig. S14 (a-b)**. Furthermore, EDS analysis confirmed negligible sodium and chloride content, revealing the high removal efficiency of NaCl crystal from PDA NWs-NF surface **Fig. S14 (c)**. The good reusability results, and excellent self-cleaning properties are attributed to; (1) the large number of hydroxyl and carboxyl groups in PDA, which absorb the water rapidly through its superhydrophilicity, leading to fast salt dissolving [48], (2) the weak adhesion between the salt crystals and PDA NWs on NF [49], and (3) the 3D porous interconnected structure of NF provides more spaces so that the concentrated and diluted brine in the pores can spontaneously form convection and diffusion. Overall, our solar evaporator displayed good salt resistance making it potentially applicable for solar seawater desalination.

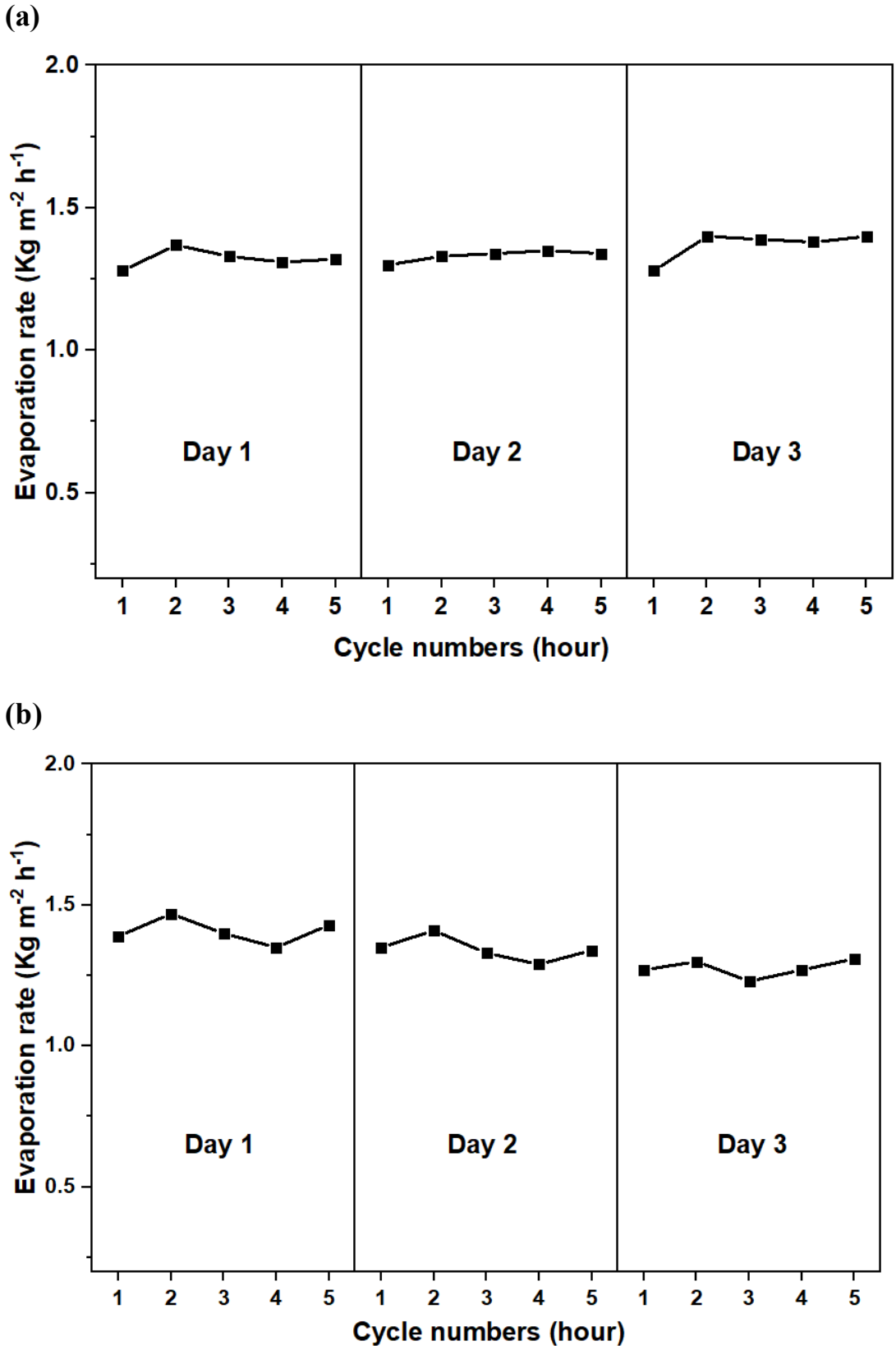

Fig. 9 Cycling stability of PDA NWs-NF based evaporator. The evaporation rate during a static-continuous light irradiation for 3 days; **(a)** real seawater. **(b)** High saline brine (75 g NaCl/L).

The self-cleaning properties were assessed by examining the self-desalting capability of our proposed NWs PDA-NF based solar evaporator. During the test, 1 g of NaCl was placed on the NWs PDA-NF surface, and natural seawater was used as a feed. The test was performed under simulated sunlight (one sun) and dark conditions. After placing the salt at the top of the NWs PDA-NF surface, the salt started to dissolve within 15 s. This could be mainly attributed to the superhydrophilicity of NWs PDA-NF, resulting in a fast water supply. Under dark conditions, most of the salt disappeared within 170 min, until no salt was realized on the surface after 270 minutes (**Fig. 10 a**). Upon sunlight illumination, the salt starts gradually to dissolve, penetrate and diffuse within the pores of the substrate. Finally, no salt was noticed on the surface after 50 min (**Fig 10 b**). The obtained results were compared to the control sample TNF (without PDA). The amount of NaCl on the NF surface did not change much under dark conditions or sunlight (**Figure 10 c,d**). This is mainly derived from surface hydrophobicity, which reduces the water supply from the bottom surface. Besides, the absence of the coated solar absorber PDA results in low-solar-thermal conversions and, hence, low water evaporation and vapor escape. The observations mentioned above reveal PDA's importance for achieving good self-cleaning properties for solar-driven seawater desalination.

(a)

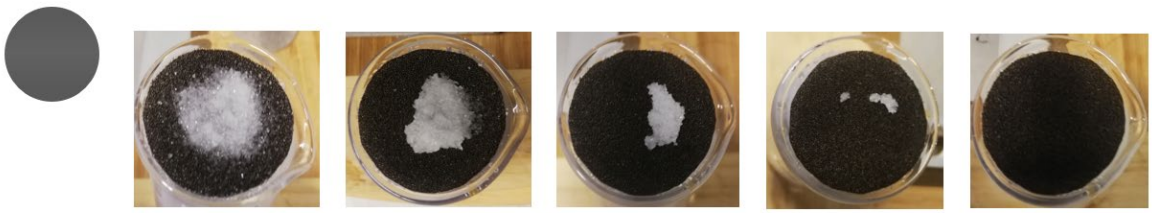

15 seconds **40 minutes** **100 minutes** **170 minutes** **270 minutes**

(b)

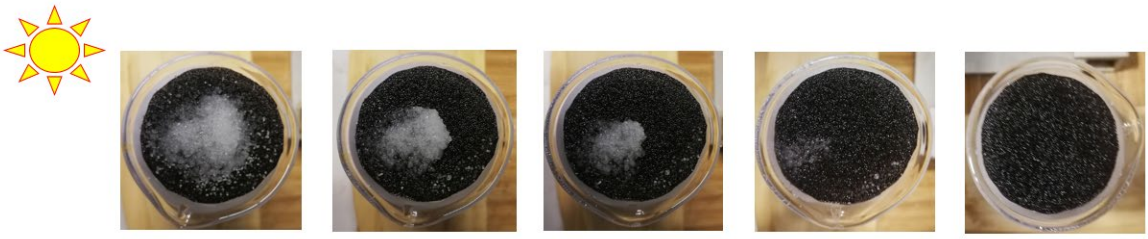

15 seconds **10 minutes** **20 minutes** **40 minutes** **50 minutes**

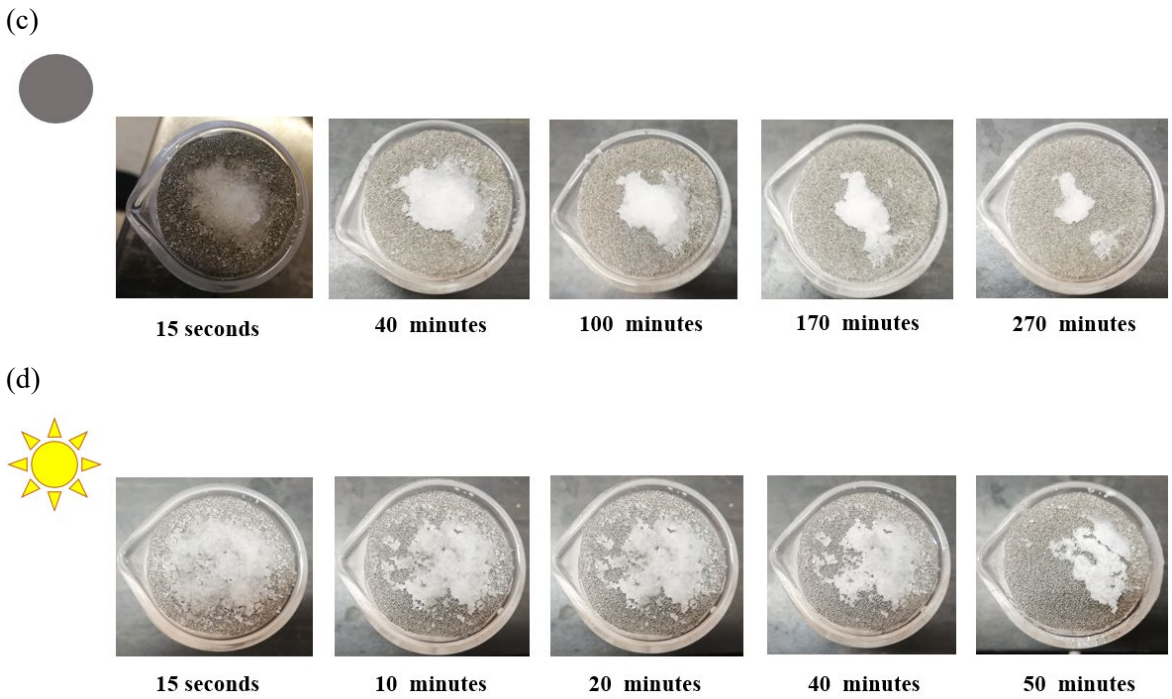

Fig. 10 Fig. 10 Self-cleaning properties of; PDA NWs-NF (a) in dark conditions (without sunlight), (b) under one sun intensity. Treated NF (c) in dark conditions (without sunlight), (d) under one sun intensity.

Conclusion

PDA NWs-NF were prepared using a straightforward and scalable *in situ* oxidative polymerization. Our work explored the superior hydrophilicity and the perks of interconnected surfaces of the 3D porous hierarchical PDA NWs. Excellent solar absorption capability covering the main solar spectrum region and efficient photothermal conversion was demonstrated. PDA NWs-NF based evaporator confirms a remarkable water evaporation rate of 1.39 kg m^{-2} h^{-1} and efficiency of 87.2%, which could be achieved under 1 sun illumination. Moreover, PDA NWs-NF based evaporators display excellent salt ions rejection meeting the standard required for drinking water. Notably, by taking advantage of the thicker PDA containing hydrophilic hydroxyl groups, exceptional durability and stability could obtain using real seawater and high brine salinity. Even after 3 days (5 cycles/day), the evaporation performance was not much deviated from the initial evaporation performance. Additionally,

the tiny salt formed on the surface during desalination can be simply re-washed by immersing in DIW. The salt resistance of our designed materials could be attributed to the weak adhesion of salts on the PDA-NF surface. Besides, the self-cleaning properties can be realized through chemical advection and diffusion. The aforementioned attributes suggested the effectiveness of our proposed PDA NWs-NF in seawater desalination. Our proposed approach is simple and scalable for fabricating large-scale solar evaporators for both portable solar devices for solar-driven seawater purification.

Acknowledgments

Idris Ibrahim is grateful for the financial support from the Australian Government through the International Research Training Program (IRTP) Scholarship for his PhD studies. The team appreciates the support from the UTS Cross-Faculty Collaboration Scheme (PRO21-12429) and from the Australia Research Council Industrial Transformation Research Hubs. Authors would also like to acknowledge Dr. Alaina Ammit and Dr. Katie McBean for their assistance in providing the laboratory access.

CRediT authorship contribution statement

Idris Ibrahim: Conceptualization, Methodology, Formal Analysis, Visualization, Data curation, Writing-original draft, Investigation, Writing & editing. **Syed Mukit Hossein**: Visualization, review & editing. **Dong Han Seo:** Data curation, review & editing. **Tim Foster**: Review and editing; **Andrew McDonagh:** Supervision, review & editing. **Hokyong Shon:** Supervision, visualization, Investigation, review & editing. **Leonard Tijing:** Supervision, data curation, visualization, funding support, investigation, planning, review & editing.

References

1. Rijsberman, F.R., *Water scarcity: fact or fiction?* Agricultural water management, 2006. **80**(1-3): p. 5-22.
2. Prüss, A., et al., *Estimating the burden of disease from water, sanitation, and hygiene at a global level.* Environmental health perspectives, 2002. **110**(5): p. 537-542.
3. Chen, T.-C. and C.-D. Ho, *Immediate assisted solar direct contact membrane distillation in saline water desalination.* Journal of Membrane Science, 2010. **358**(1-2): p. 122-130.
4. Wang, Z., et al., *Pathways and challenges for efficient solar-thermal desalination.* Science advances, 2019. **5**(7): p. eaax0763.
5. Ibrahim, I., et al., *Semiconductor photothermal materials enabling efficient solar steam generation toward desalination and wastewater treatment.* Desalination, 2020: p. 114853.
6. Zhu, X., et al., *Metal organic framework enabled wood evaporator for solar-driven water purification.* Separation and Purification Technology, 2022. **281**: p. 119912.
7. Meng, X., et al., *Coupling of hierarchical Al2O3/TiO2 nanofibers into 3D photothermal aerogels toward simultaneous water evaporation and purification.* Advanced Fiber Materials, 2020. **2**(2): p. 93-104.
8. Ibrahim, I., et al., *Biomass-based photothermal materials for interfacial solar steam generation: A review.* Materials Today Energy, 2021: p. 100716.
9. Guo, C., et al., *Constructing 3D optical absorption holes by stacking macroporous membrane for highly efficient solar steam generation.* Renewable Energy, 2020. **159**: p. 944-953.
10. Zhao, H.-Y., et al., *Lotus-inspired evaporator with Janus wettability and bimodal pores for solar steam generation.* Cell Reports Physical Science, 2020. **1**(6): p. 100074.
11. Chen, X., et al., *Resilient biomass-derived hydrogel with tailored topography for highly efficient and long-term solar evaporation of high-salinity brine.* Journal of Materials Chemistry A, 2020. **8**(43): p. 22645-22656.
12. Li, H., et al., *Latest development in salt removal from solar-driven interfacial saline water evaporators: Advanced strategies and challenges.* Water Research, 2020. **177**: p. 115770.
13. Liu, F., et al., *Superwetting monolithic hypercrosslinked polymers nanotubes with high salt-resistance for efficient solar steam generation.* Solar Energy Materials and Solar Cells, 2021. **221**: p. 110913.
14. Wang, S., et al., *Potentially scalable fabrication of salt-rejection evaporator based on electrogenerated polypyrrole-coated nickel foam for efficient solar steam generation.* Desalination, 2021. **505**: p. 114982.
15. Wei, D., et al., *Ionic hyper-cross-linked polymers monoliths for efficient solar steam generation.* European Polymer Journal, 2021. **147**: p. 110281.
16. Chen, Z., et al., *Microgroove-Structured PDA/PEI/PPy@ PI-MS Photothermal Aerogel with a Multilevel Water Transport Network for Highly Salt-Rejecting Solar-Driven Interfacial Evaporation.* ACS Applied Materials & Interfaces, 2021.
17. Peng, F., et al., *A janus solar evaporator with 2D water path for highly efficient salt-resisting solar steam generation.* Solar Energy Materials and Solar Cells, 2021. **221**: p. 110910.
18. Wang, F., et al., *Salt-Resistant Photothermal Materials Based on Monolithic Porous Ionic Polymers for Efficient Solar Steam Generation.* ACS Applied Energy Materials, 2020. **3**(9): p. 8746-8754.
19. Xiao, C., et al., *Janus poly (ionic liquid) monolithic photothermal materials with superior salt-rejection for efficient solar steam generation.* ACS Applied Energy Materials, 2019. **2**(12): p. 8862-8870.
20. Huang, L., et al., *Laser-Engineered Graphene on Wood Enables Efficient Antibacterial, Anti-Salt-Fouling, and Lipophilic-Matter-Rejection Solar Evaporation.* ACS applied materials & interfaces, 2020. **12**(46): p. 51864-51872.

21. Li, J., et al., *Migration crystallization device based on biomass photothermal materials for efficient salt-rejection solar steam generation.* ACS Applied Energy Materials, 2020. **3**(3): p. 3024-3032.
22. Cendrowski, K., et al., *The river water influence on cationic and anionic dyes collection by nickel foam with carbonized metal-organic frameworks and carbon nanotubes.* Journal of Alloys and Compounds, 2021. **876**: p. 160093.
23. Edison, T.N.J.I., et al., *A novel binder-free electro-synthesis of hierarchical nickel sulfide nanostructures on nickel foam as a battery-type electrode for hybrid-capacitors.* Fuel, 2020. **276**: p. 118077.
24. Liu, H., et al., *CoWO4–x-Based Photothermal Membranes for Solar-Driven Water Evaporation and Eutrophic Lake Water Purification.* ACS omega, 2020. **5**(49): p. 31598-31607.
25. Jiang, H., et al., *Broadband nickel sulfide/nickel foam-based solar evaporator for highly efficient water purification and electricity generation.* ACS Sustainable Chemistry & Engineering, 2020. **8**(29): p. 10833-10841.
26. Ren, H., et al., *Hierarchical graphene foam for efficient omnidirectional solar–thermal energy conversion.* Advanced Materials, 2017. **29**(38): p. 1702590.
27. Gong, L., et al., *Highly Efficient Solar Evaporator Based on Graphene/MoO3-x Coated Porous Nickel for Water Purification.* Separation and Purification Technology, 2021: p. 119139.
28. Han, S., et al., *Flame synthesis of superhydrophilic carbon nanotubes/Ni foam decorated with Fe2O3 nanoparticles for water purification via solar steam generation.* ACS applied materials & interfaces, 2020. **12**(11): p. 13229-13238.
29. Zou, Y., et al., *Boosting solar steam generation by photothermal enhanced polydopamine/wood composites.* Polymer, 2021. **217**: p. 123464.
30. Lee, H., et al., *Mussel-inspired surface chemistry for multifunctional coatings.* science, 2007. **318**(5849): p. 426-430.
31. Zou, Y., et al., *Regulating the absorption spectrum of polydopamine.* Science advances, 2020. **6**(36): p. eabb4696.
32. Liu, Y., K. Ai, and L. Lu, *Polydopamine and its derivative materials: synthesis and promising applications in energy, environmental, and biomedical fields.* Chemical reviews, 2014. **114**(9): p. 5057-5115.
33. Barclay, T.G., et al., *Versatile surface modification using polydopamine and related polycatecholamines: Chemistry, structure, and applications.* Advanced Materials Interfaces, 2017. **4**(19): p. 1601192.
34. Fang, Y., et al., *Eco-friendly colorization of textile originating from polydopamine nanofilm structural color with high colorfastness.* Journal of Cleaner Production, 2021. **295**: p. 126523.
35. Zhou, W., et al., *A facile method for the fabrication of a superhydrophobic polydopamine-coated copper foam for oil/water separation.* Applied Surface Science, 2017. **413**: p. 140-148.
36. Mascaretti, L., et al., *Solar steam generation on scalable ultrathin thermoplasmonic TiN nanocavity arrays.* Nano Energy, 2021. **83**: p. 105828.
37. Shan, X., et al., *Porous reduced graphene oxide/nickel foam for highly efficient solar steam generation.* Nanotechnology, 2019. **30**(42): p. 425403.
38. Wang, T., et al., *Three-dimensional hierarchical oxygen vacancy-rich WO3-decorated Ni foam evaporator for high-efficiency solar-driven interfacial steam generation.* Journal of Colloid and Interface Science, 2021. **602**: p. 767-777.
39. Wang, P., et al., *Co3O4 nanoforest/Ni foam as the interface heating sheet for the efficient solar-driven water evaporation under one sun.* Sustainable Materials and Technologies, 2019. **20**: p. e00106.
40. Galeotti, G., et al., *Synthesis of mesoscale ordered two-dimensional π-conjugated polymers with semiconducting properties.* Nature Materials, 2020. **19**(8): p. 874-880.

41. Venz, S. and B. Dickens, *NIR-spectroscopic investigation of water sorption characteristics of dental resins and composites.* Journal of biomedical materials research, 1991. **25**(10): p. 1231-1248.
42. Ibrahim, I., et al., *3D microflowers CuS/Sn2S3 heterostructure for highly efficient solar steam generation and water purification.* Solar Energy Materials and Solar Cells, 2021. **232**: p. 111377.
43. Shi, Y., et al., *A Robust CuCr2O4/SiO2 Composite Photothermal Material with Underwater Black Property and Extremely High Thermal Stability for Solar-Driven Water Evaporation.* Advanced Sustainable Systems, 2018. **2**(3): p. 1700145.
44. Fan, H., et al., *A design of bifunctional photothermal layer on polysulfone membrane with enclosed cellular-like structure for efficient solar steam generation.* Chemical Engineering Journal, 2021. **415**: p. 128798.
45. Zhao, X., et al., *Macroporous three-dimensional MXene architectures for highly efficient solar steam generation.* Journal of Materials Chemistry A, 2019. **7**(17): p. 10446-10455.
46. Tian, Y., et al., *Farm-waste-derived recyclable photothermal evaporator.* Cell Reports Physical Science, 2021: p. 100549.
47. Zhao, S., et al., *Functional oil-repellent photothermal materials based on nickel foam for efficient solar steam generation.* Solar Energy Materials and Solar Cells, 2020. **214**: p. 110574.
48. Feng, J., et al., *Low-cost and facile hydrophilic amplification of raw corn straws for the applications of highly efficient interfacial solar steam generation.* Materials Chemistry and Physics, 2021. **271**: p. 124904.
49. Peng, H., D. Wang, and S. Fu, *Artificial transpiration with asymmetric photothermal textile for continuous solar-driven evaporation, spatial salt harvesting and electrokinetic power generation.* Chemical Engineering Journal, 2021. **426**: p. 131818.

Supplementary information

Insight into the role of polydopamine nanostructures on nickel foam-based photothermal materials for solar water evaporation

Idris Ibrahim[a], Sayed Mukit Hossain[a], Dong Han Seo[a,b], Andrew McDonagh[c], Tim Foster[d], Ho Kyong Shon[a,e], Leonard Tijing[a,e,*]

[a]Centre for Technology in Water and Wastewater, School of Civil and Environmental Engineering, University of Technology Sydney, PO Box 123, 15 Broadway, Sydney, NSW, 2007, Australia

[b]Energy Materials & Devices, Korea Institute of Energy Technology (KENTECH), Naju, Republic of Korea

[c]School of Mathematical and Physical Sciences, University of Technology Sydney, Ultimo 2007, Australia

[d]Institute for Sustainable Futures, University of Technology Sydney, Ultimo, NSW, Australia

[e]ARC Research Hub for Nutrients in a Circular Economy, University of Technology Sydney, PO Box 123, 15 Broadway, Sydney, NSW, 2007, Australia

[*]Corresponding author: L.D. Tijing; email: leonard.tijing@uts.edu.au

Fig. S1. Photo-image of the designed PDA NWs driven solar evaporator.

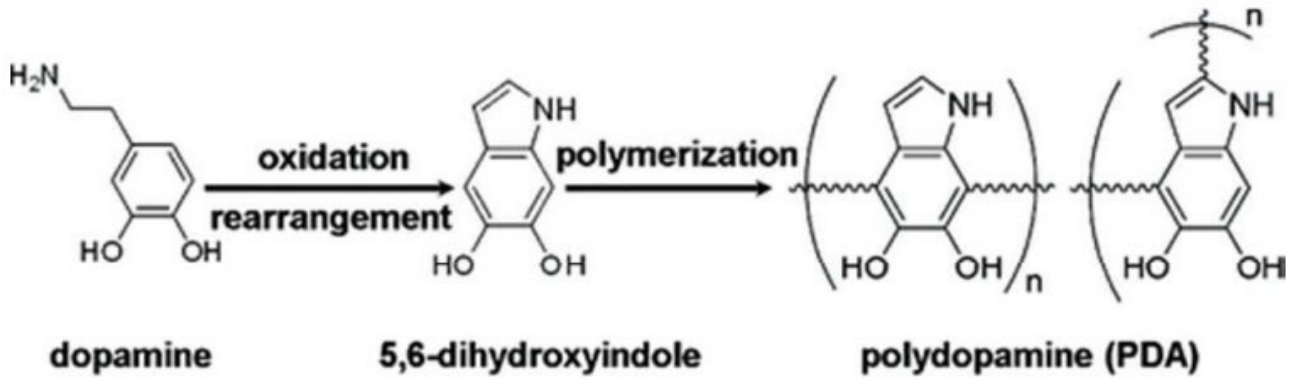

Fig. S2. Michael oxidation reaction of dopamine to polydopamine (PDA) [1].

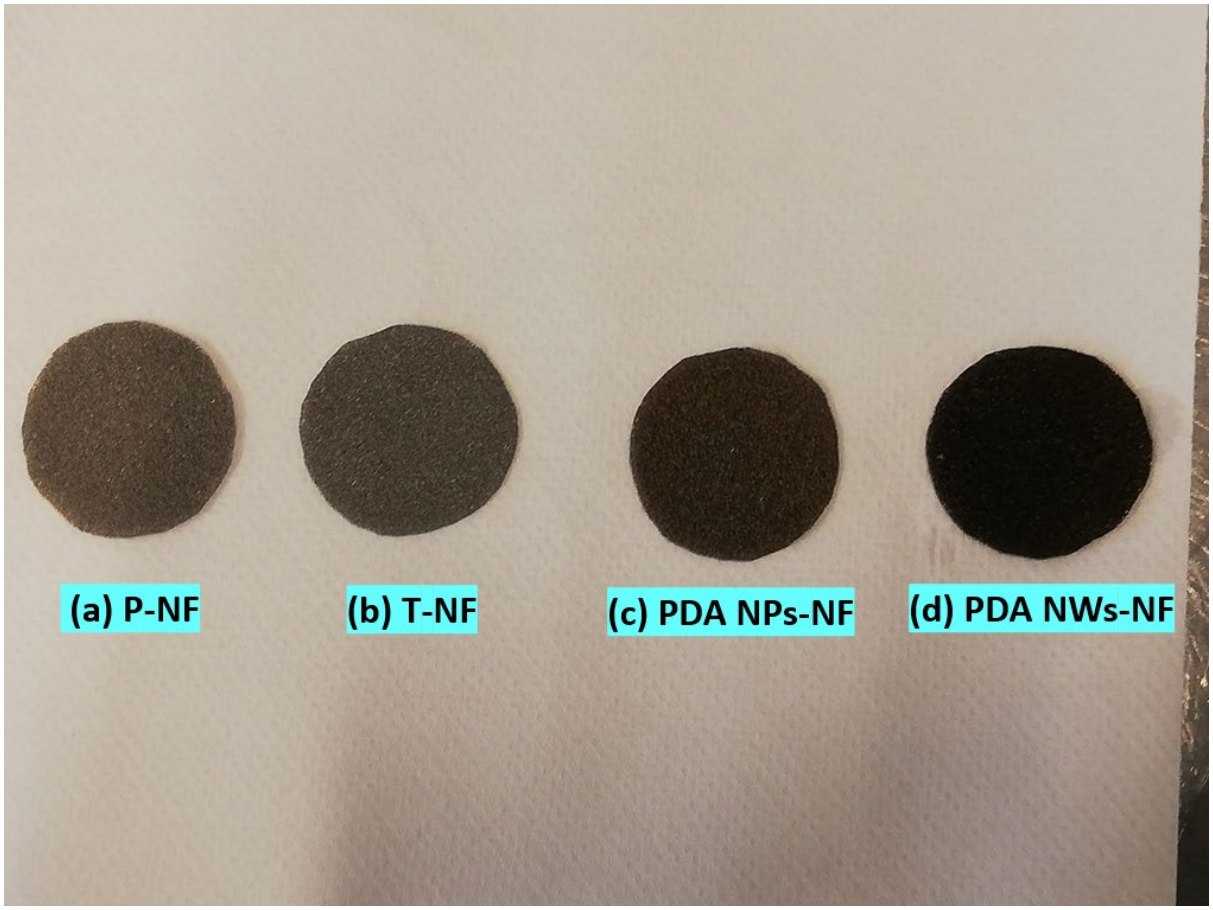

Fig. S3. Photo-images of **(a)** Pristine NF, **(b)** treated NF, **(c)** PDA-NPs-NF, and **(d)** PDA-NWs-NF

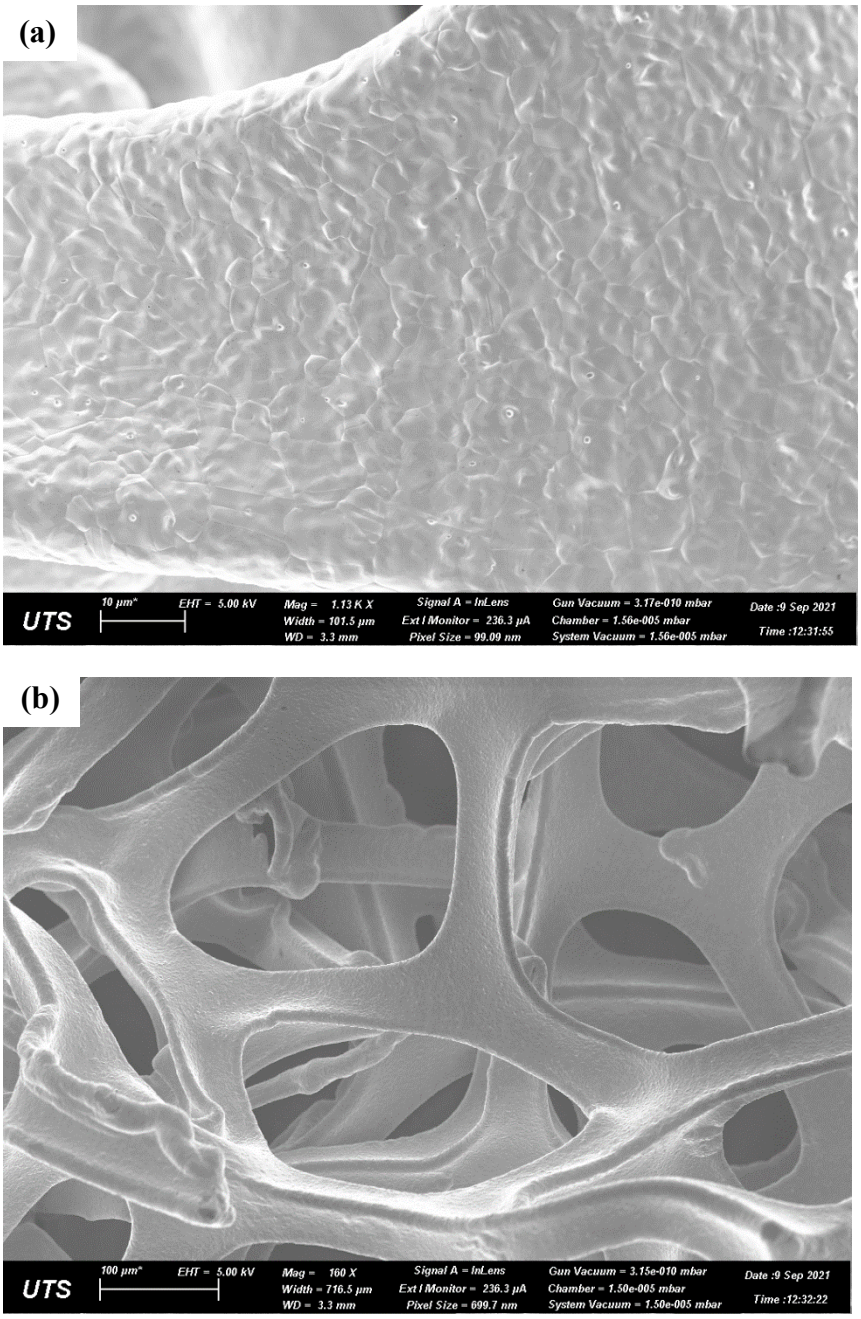

Fig. S4. SEM images of pristine NF **(a)** High magnification. **(b)** Low magnification.

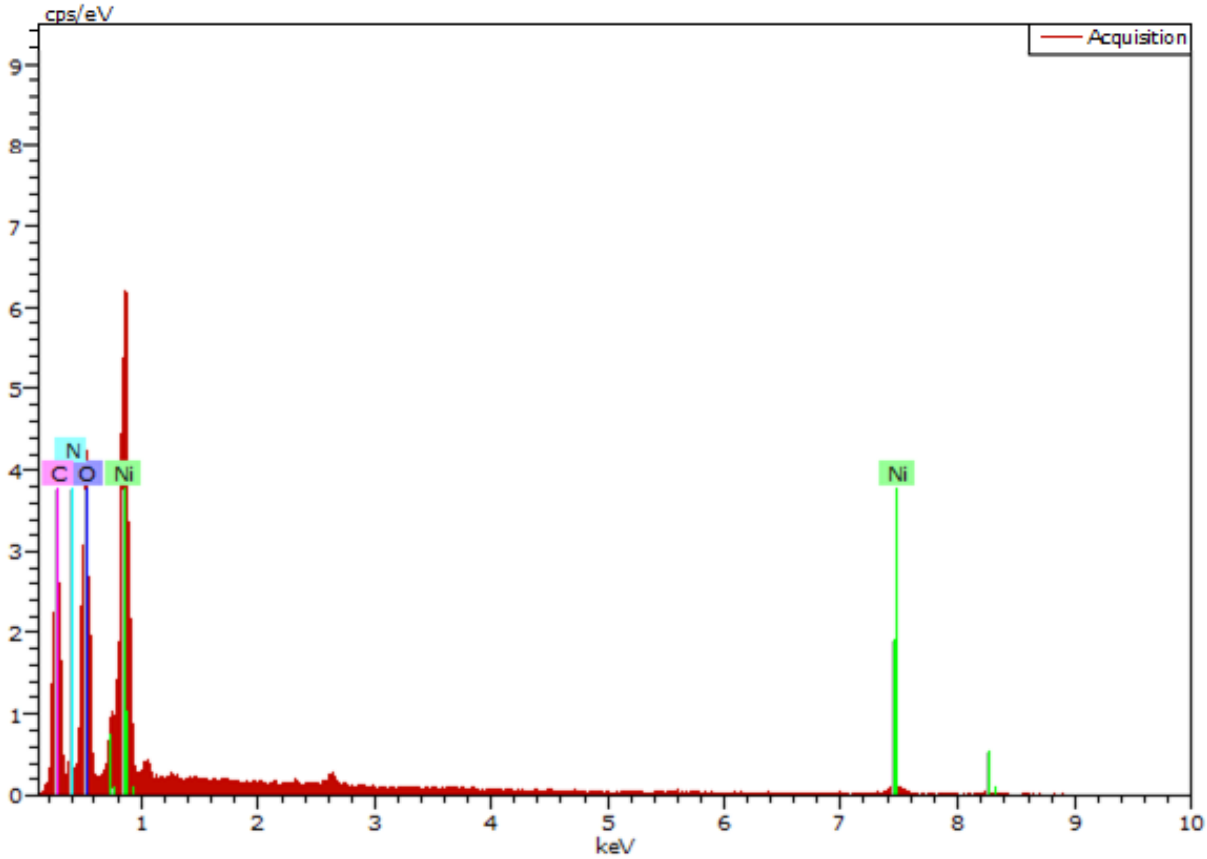

Spectrum: Acquisition

El	AN	Series	unn. C [wt.%]	norm. C [wt.%]	Atom. C [at.%]	Error (1 Sigma) [wt.%]
C	6	K-series	26.59	26.59	44.83	3.64
N	7	K-series	4.91	4.91	7.10	1.04
O	8	K-series	26.55	26.55	33.60	3.54
Ni	28	L-series	41.95	41.95	14.47	5.20
		Total:	100.00	100.00	100.00	

Fig. S5. EDS analysis of NF-PDA NWs.

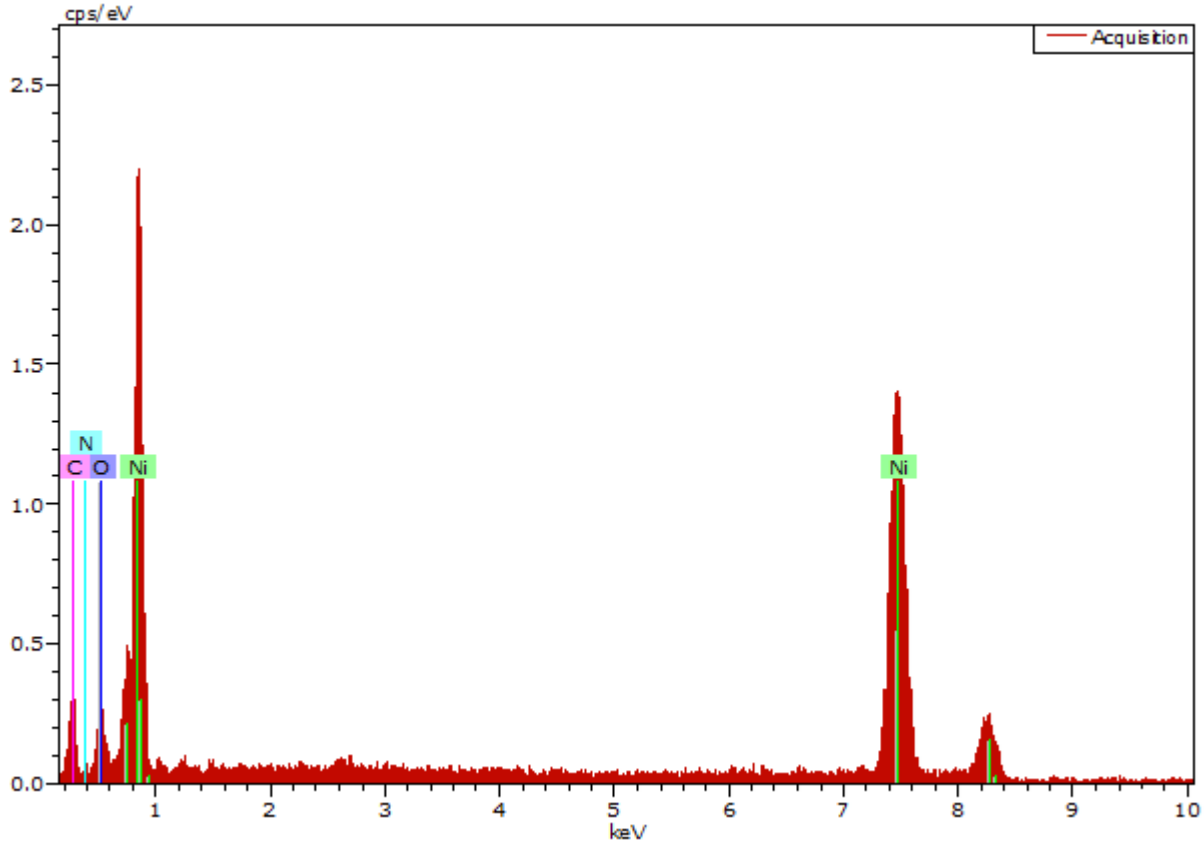

Spectrum: Acquisition

El	AN	Series	unn. C [wt.%]	norm. C [wt.%]	Atom. C [at.%]	Error (1 Sigma) [wt.%]
C	6	K-series	17.54	8.60	29.49	3.85
N	7	K-series	1.69	0.83	2.44	0.80
O	8	K-series	4.95	2.43	6.24	1.19
Ni	28	K-series	179.70	88.14	61.83	5.79
		Total:	203.87	100.00	100.00	

Fig. S6. EDS analysis of NF-PDA NPs.

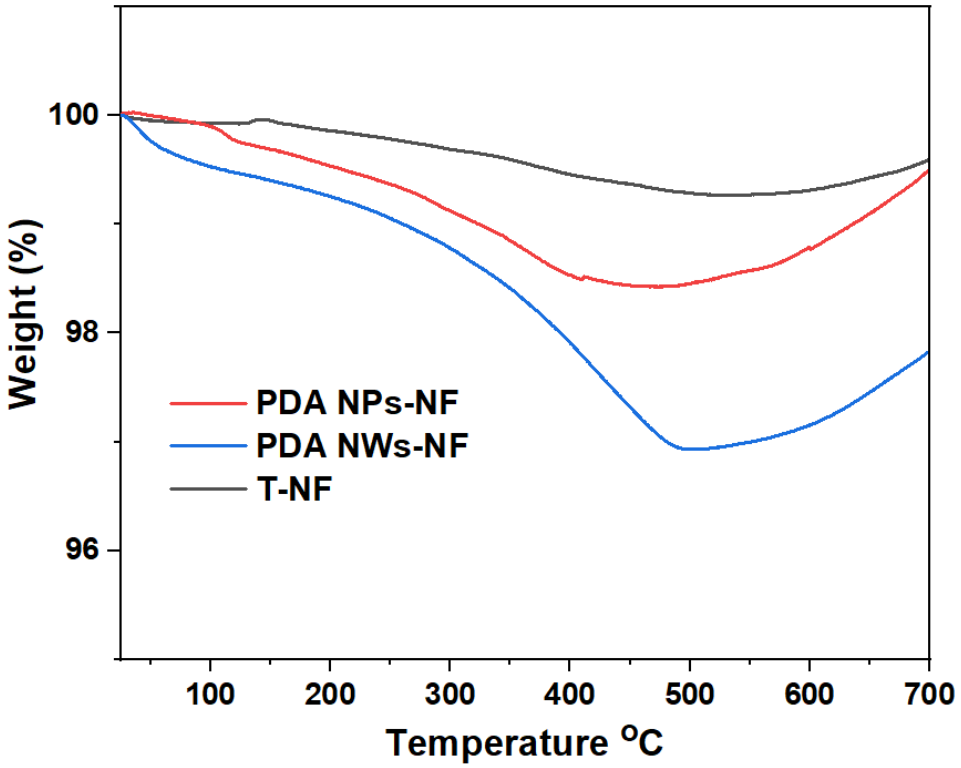

Fig S7. TGA analysis of NF, PDA NPs-NF and PDA NWs-NF.

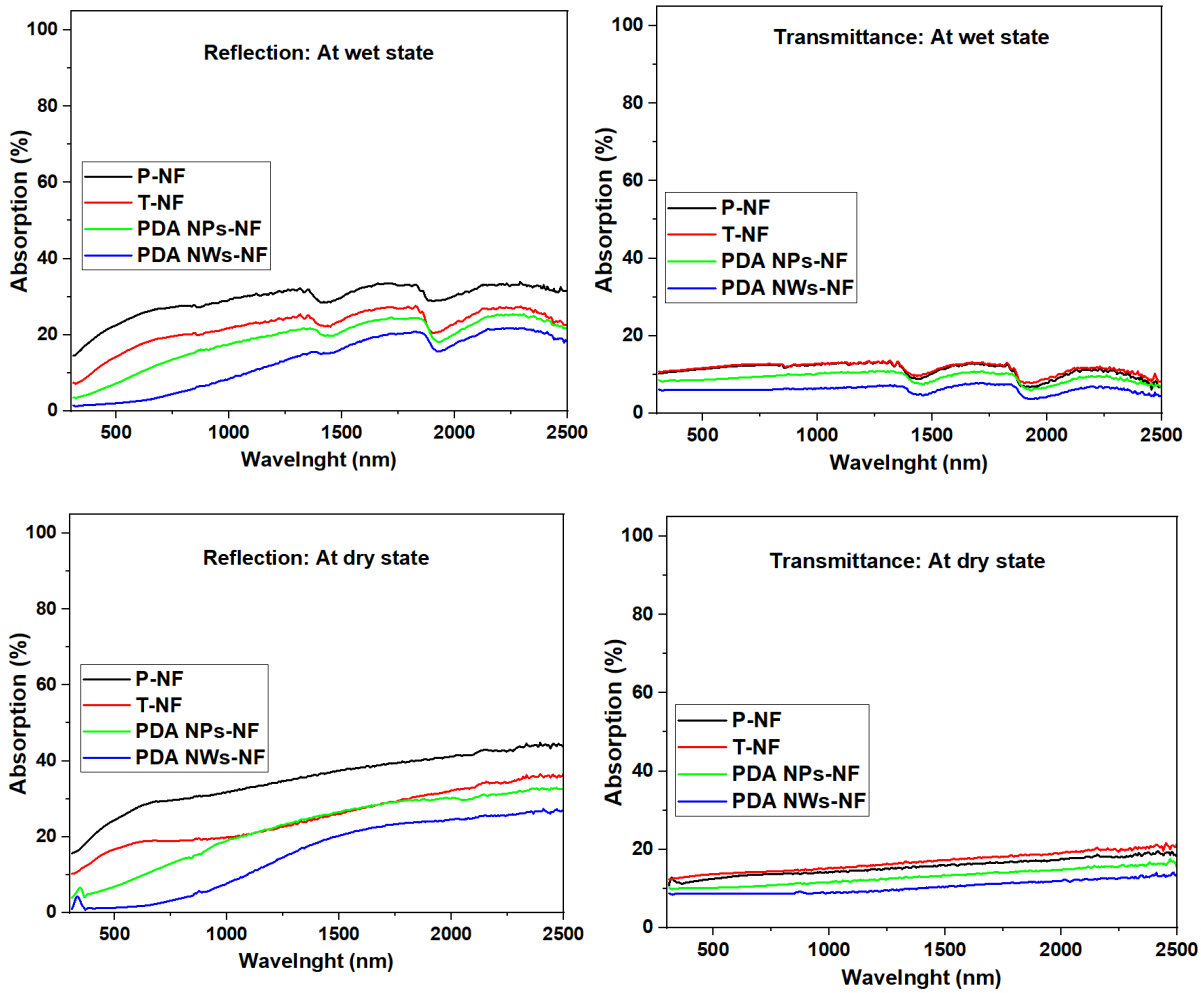

Fig S8. The light reflection and transmittance at wet state and dry state

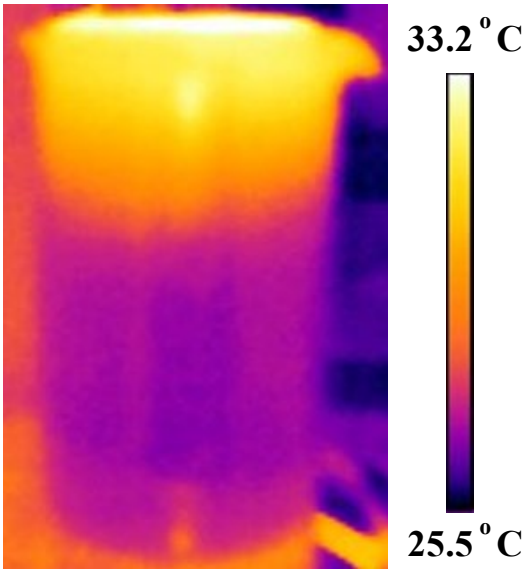

Fig S9. Side photo of NWs PDA-NF based solar evaporator system upon sunlight irradiation for 15 minutes.

Water condensation and collection

We used a similar solar evaporator that was described in Fig 2 a. For water condensation, we just placed a larger beaker on the top of the evaporator. After sunlight irradiation, the water evaporator started to be heated, and the vapor was released and rose higher to the covered glass beaker. Then, it will be collected and taken for further quantitative analysis.

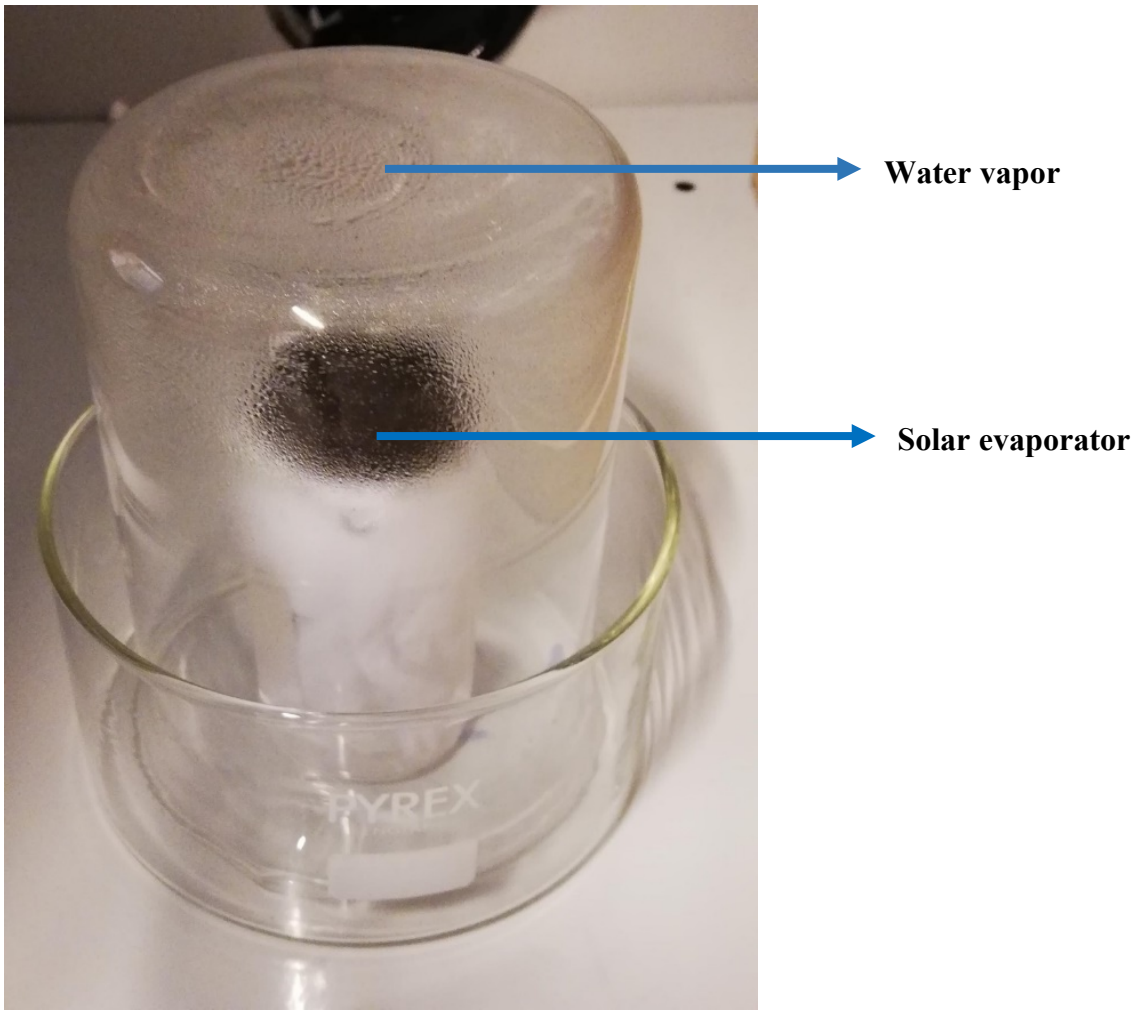

Fig S10. Home-made device of PDA NWs-NF based evaporator for water collection [42].

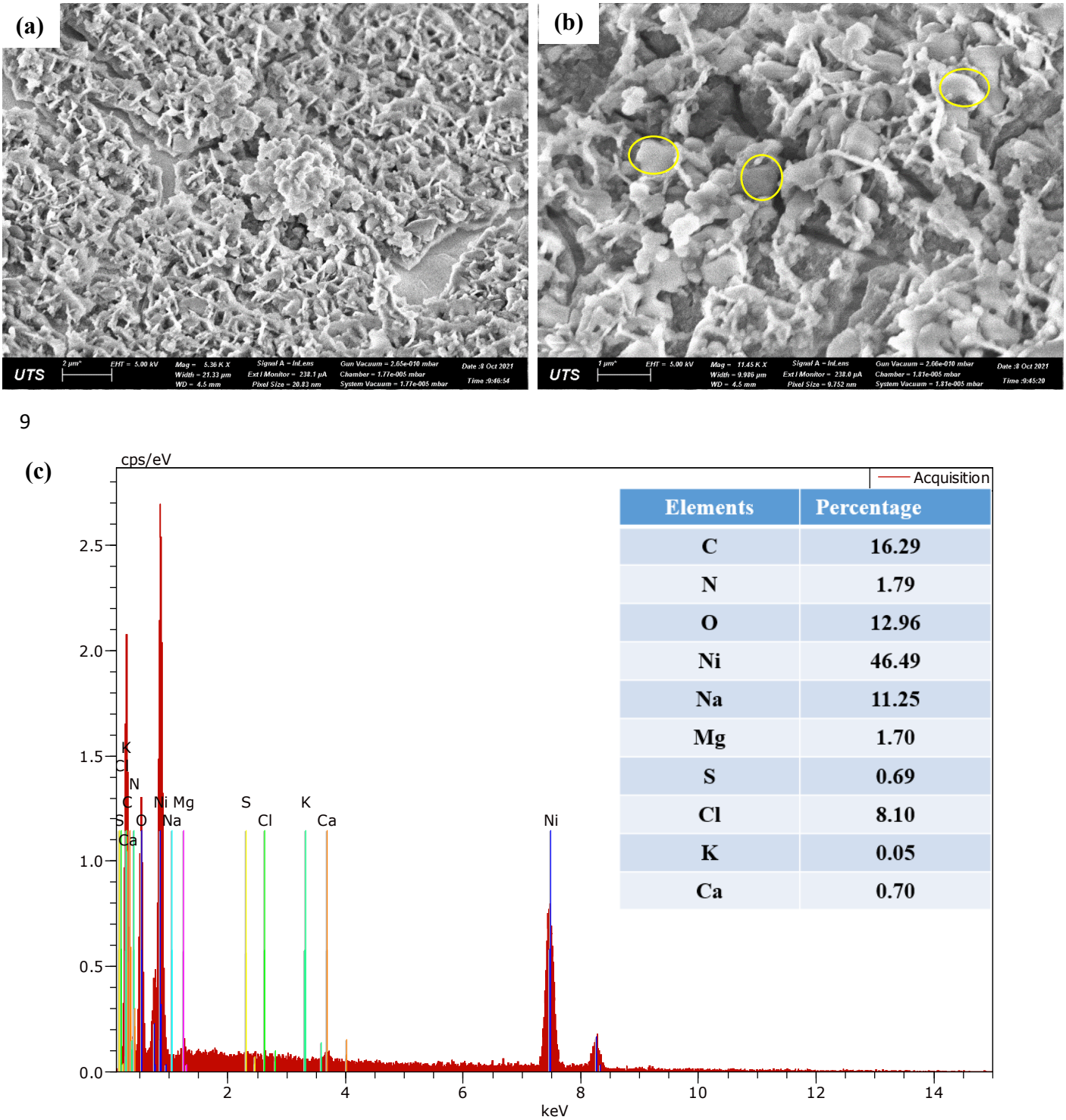

Elements	Percentage
C	16.29
N	1.79
O	12.96
Ni	46.49
Na	11.25
Mg	1.70
S	0.69
Cl	8.10
K	0.05
Ca	0.70

Fig S11. (a-b) SEM images of PDA NWs-NF, after 3 Days solar desalination test using real seawater, and **(c)** corresponding EDS analysis.

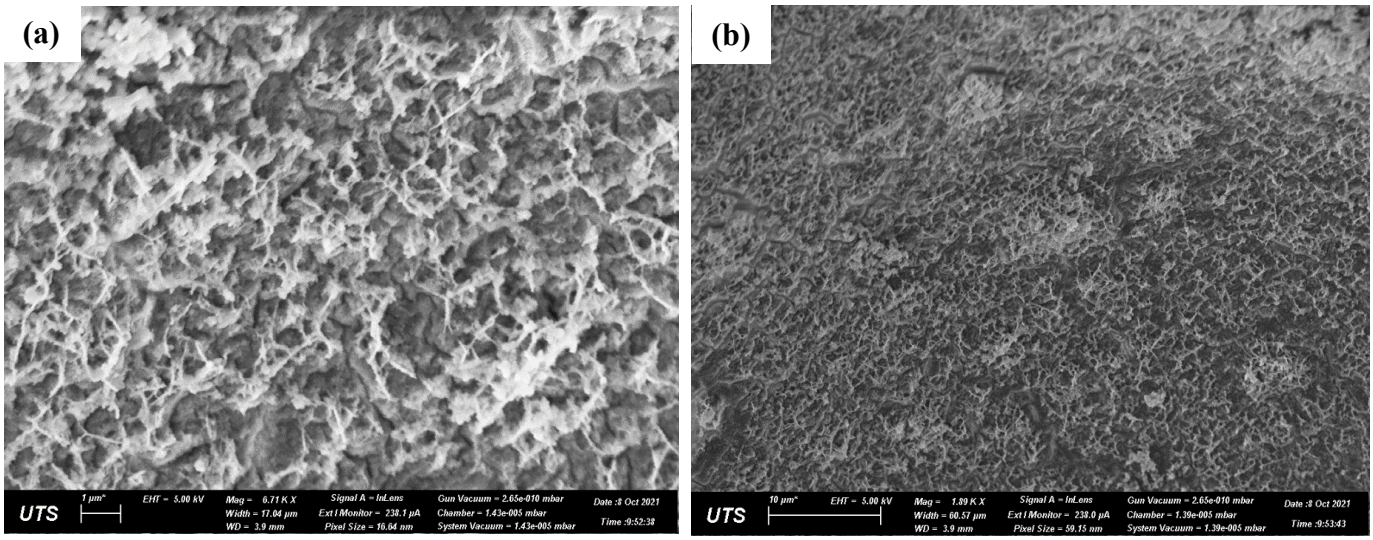

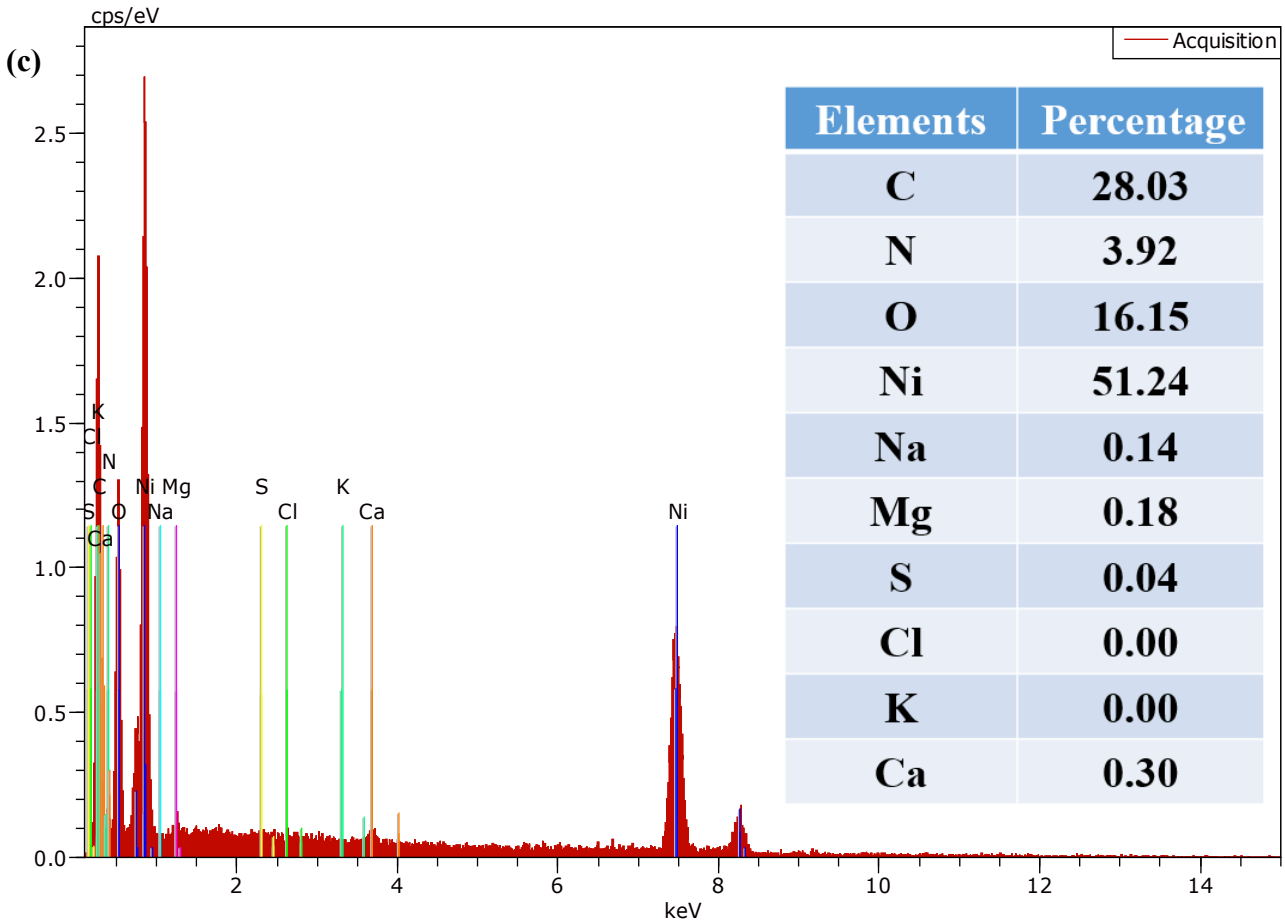

Elements	Percentage
C	28.03
N	3.92
O	16.15
Ni	51.24
Na	0.14
Mg	0.18
S	0.04
Cl	0.00
K	0.00
Ca	0.30

Fig S12. (a,b) SEM images of NF-PDA NWs after washing by soaking in DIW for 9 hours, after 3 Days solar desalination test using real seawater, and. **(c)** corresponding EDS analysis.

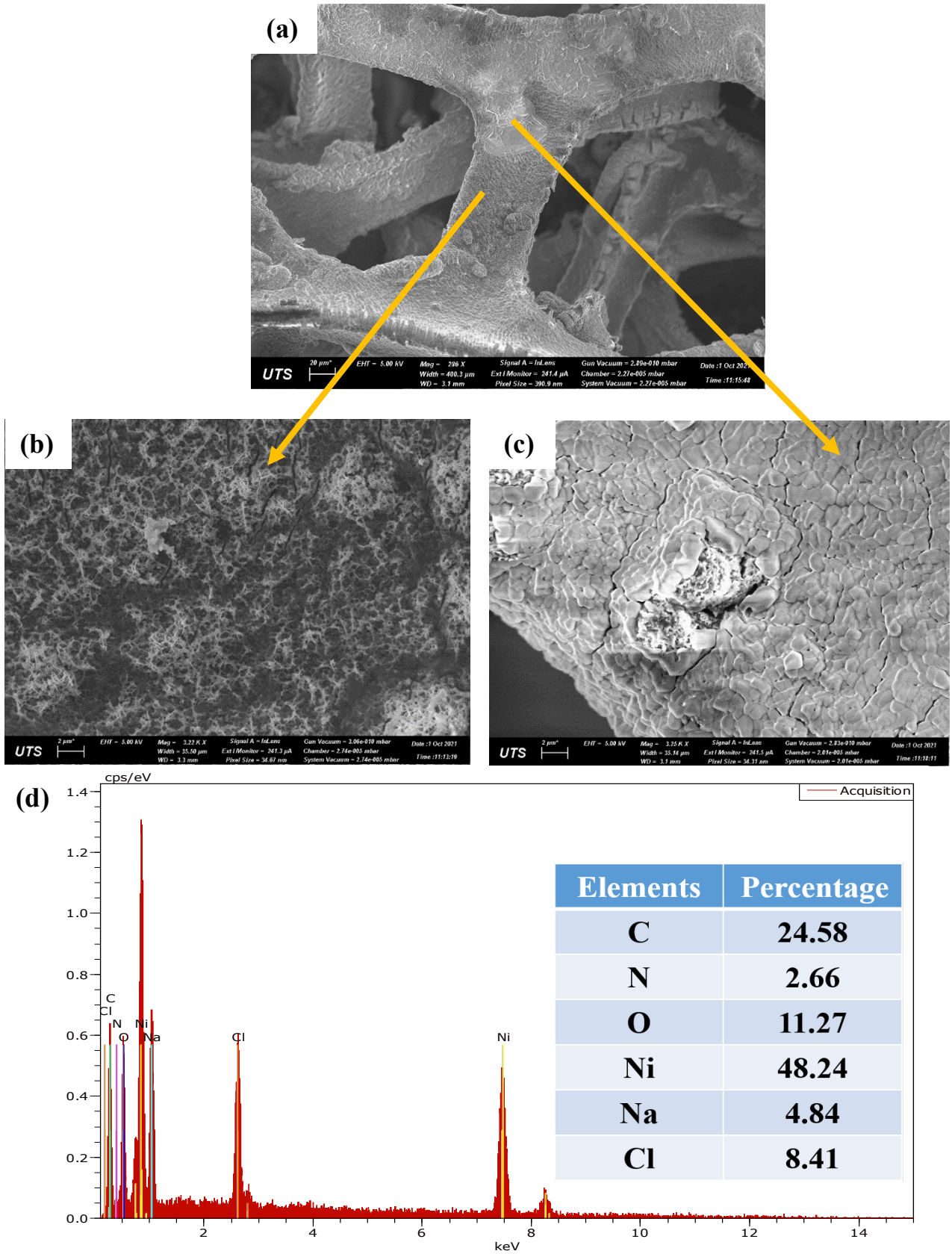

Elements	Percentage
C	24.58
N	2.66
O	11.27
Ni	48.24
Na	4.84
Cl	8.41

Fig S13. (a-c) SEM images of NF-PDA NWs, after 3 Days solar desalination test using (brine solution (75 g/L NaCl), and **(d)** corresponding EDS analysis.

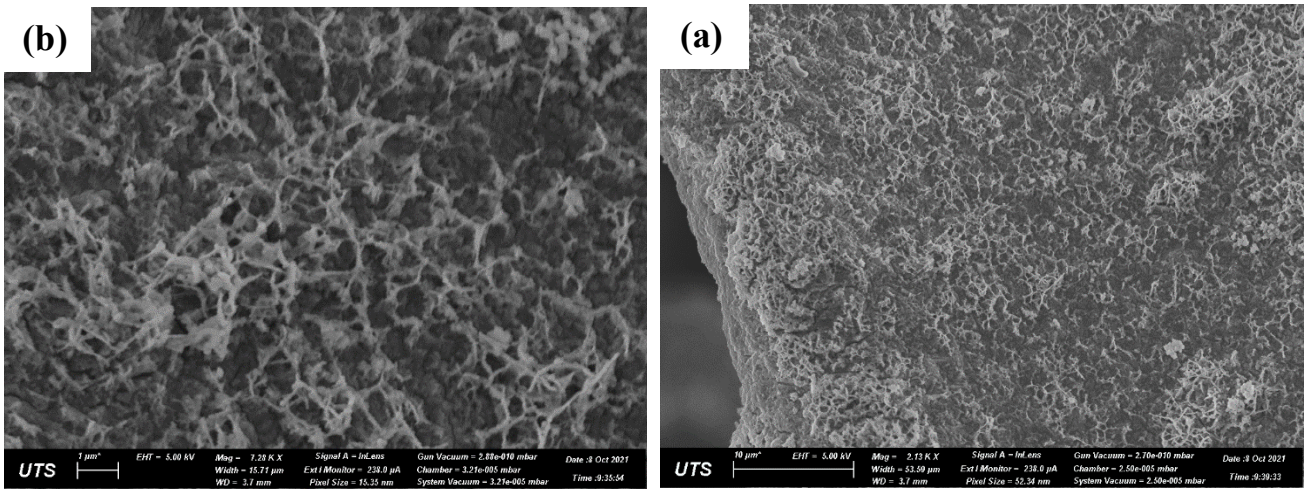

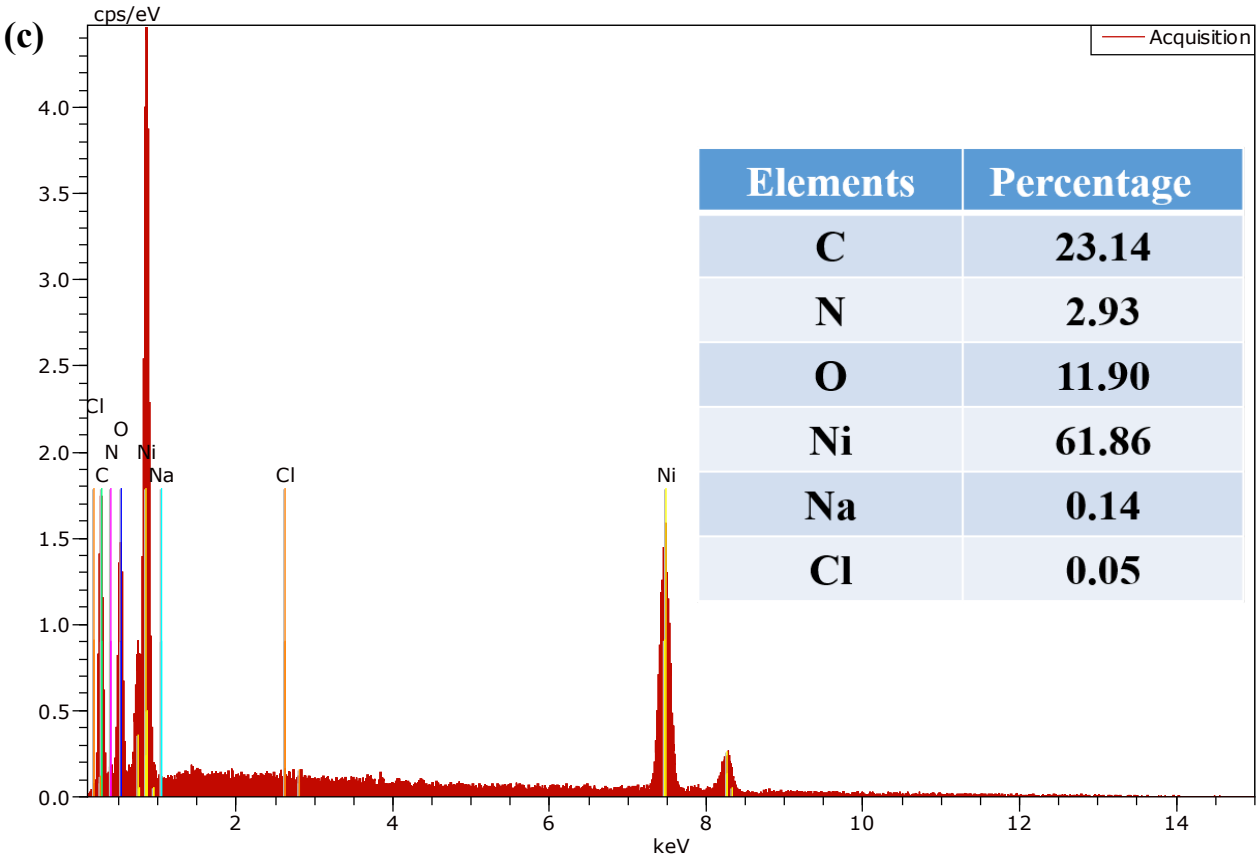

Elements	Percentage
C	23.14
N	2.93
O	11.90
Ni	61.86
Na	0.14
Cl	0.05

Fig S14. (a,b) SEM images of NF-PDA NWs after washing by soaking in DIW for 9 hours, after 3 Days solar desalination test using high brine solution (75 g/L NaCl), and **(c)** corresponding EDS analysis.

Table S1. Comparison of recent reported results on NF derived solar evaporator

Material	**Water evaporation rate kg m^{-2} h^{-1} (under one sun)**	**References**
Oil repellent modified-S-NF	1.33	[2]
Polypyrrole- NF - Polyurethane sponge	1.44	[3]
3D hierarchical WO_{3-x} NF	1.50	[4]
Porous reduced graphene oxide/ NF	1.33	[5]
Nickel sulfide/nickel foam	1.29	[6]
Hierarchical graphene foam	1.4	[7]
Fe_2O_3/CNT/ NF	1.48	[8]
Graphene/MoO_3-x Coated Porous NF	1.50	[9]
Polydopamine nanowires/ NF	1.39	This study

References

1. Batul, R., et al., *Recent progress in the biomedical applications of polydopamine nanostructures.* Biomaterials science, 2017. **5**(7): p. 1204-1229.
2. Zhao, S., et al., *Functional oil-repellent photothermal materials based on nickel foam for efficient solar steam generation.* Solar Energy Materials and Solar Cells, 2020. **214**: p. 110574.
3. Wang, S., et al., *Potentially scalable fabrication of salt-rejection evaporator based on electrogenerated polypyrrole-coated nickel foam for efficient solar steam generation.* Desalination, 2021. **505**: p. 114982.
4. Wang, T., et al., *Three-dimensional hierarchical oxygen vacancy-rich WO3-decorated Ni foam evaporator for high-efficiency solar-driven interfacial steam generation.* Journal of Colloid and Interface Science, 2021. **602**: p. 767-777.
5. Shan, X., et al., *Porous reduced graphene oxide/nickel foam for highly efficient solar steam generation.* Nanotechnology, 2019. **30**(42): p. 425403.
6. Jiang, H., et al., *Broadband nickel sulfide/nickel foam-based solar evaporator for highly efficient water purification and electricity generation.* ACS Sustainable Chemistry & Engineering, 2020. **8**(29): p. 10833-10841.
7. Ren, H., et al., *Hierarchical graphene foam for efficient omnidirectional solar–thermal energy conversion.* Advanced Materials, 2017. **29**(38): p. 1702590.
8. Han, S., et al., *Flame synthesis of superhydrophilic carbon nanotubes/Ni foam decorated with Fe2O3 nanoparticles for water purification via solar steam generation.* ACS applied materials & interfaces, 2020. **12**(11): p. 13229-13238.
9. Gong, L., et al., *Highly Efficient Solar Evaporator Based on Graphene/MoO3-x Coated Porous Nickel for Water Purification.* Separation and Purification Technology, 2021: p. 119139.